NASA Contractor Report 191112

Experimentation in the Low-Density Plume of a Simulated Electrothermal Thruster for Computer Code Validation

Dana L. Meissner
University of Toledo
Toledo, Ohio

April 1993

Prepared for
Lewis Research Center
Under Grant NAG3-577

National Aeronautics and
Space Administration

EXPERIMENTATION IN THE LOW-DENSITY PLUME OF A SIMULATED ELECTROTHERMAL THRUSTER FOR COMPUTER CODE VALIDATION

Dana L. Meissner
University of Toledo
Toledo, Ohio 43606

Abstract

Pressures and flow angles are measured in the plume of a 20° half-angle, conical nozzle in vacuum with Pitot tubes and conical probes. The area of measurement in the plume ranges from the nozzle exit plane to 480 mm axially downstream and from the plume centerline to 60 mm radially. The nozzle has an exit-to-throat area ratio of 100:1 and a throat diameter of 3.2 mm. The nozzle flow exhausts to a vacuum of order 10^{-2} Pa to simulate a resistojet (an electrothermal rocket of less than 1 N of thrust) operating in space. Experimental data are given for flows of nitrogen at 55 and 68 mg/s, stagnation temperatures between 695 and 921 K, and stagnation pressures ranging from 5600 to 7100 Pa. Data are also given for argon at a rate of 68 mg/s, a stagnation temperature of 648 K, and stagnation pressures of 4500, 4750 and 4770 Pa. Measurements in the nitrogen plume are compared with computational results from a direct-simulation Monte Carlo method.

TABLE OF CONTENTS

LIST OF TABLES

LIST OF FIGURES

NOMENCLATURE

D_e	nozzle exit diameter
D_i	nozzle inlet diameter
D_p	Pitot probe outside diameter
D_t	nozzle throat diameter
$\dot{m}$	mass flow rate
M	molecular weight
$\dot{Q}$	power supplied to the cartridge heater
P_b	surrounding vacuum pressure, or back pressure
P_o	stagnation pressure
R	radial distance measured from the nozzle centerline, shown in Figure 2-6
$\overline{R}$	dimensionless radial distance, defined in Eq. (2-1)
R_L	nozzle throat longitudinal radius
Re_t	Reynolds number based on D_t and μ_o, defined in Eq. (1-1)
t_L	nozzle lip thickness
t_p	Pitot probe wall thickness
t_w	nozzle wall thickness
T_e	nozzle surface temperature near the exit plane, shown in Figure 2-1
T_m	nozzle surface temperature half way between the throat and the exit plane, shown in Figure 2-1
T_o	stagnation temperature
Z	axial distance measured from the nozzle exit plane, shown in Figure 2-6
$\overline{Z}$	dimensionless axial distance, defined in Eq. (2-1)

Greek Symbols

μ_o	dynamic viscosity based on the propellant stagnation temperature

θ	probe rotation angle measured from the nozzle centerline
θ_e	nozzle exit half-angle
θ_i	nozzle inlet half-angle

Subscripts

e	denotes diverging (exit) portion of nozzle
i	denotes converging (inlet) portion of nozzle
o	denotes stagnation property

CHAPTER I
Introduction

1.1 Introduction to Resistojets

Resistojets are small electrothermal propulsion devices which are used to control satellites and large space structures in orbit. These thrusters heat and expand neutral gases to create thrust. The thrusts generated are typically under 1 N. The flow regimes vary from continuum, at the nozzle throat, to free-molecular flow, in the far-field plume. Under typical operating conditions, the nozzle flow is highly viscous and the plume expands widely into the vacuum, with a considerable mass flux in the backward direction. With this in mind, there are concerns regarding the adverse effects this backward flow has on satellite surfaces and instrumentation [1]. These considerations are a major factor in positioning control thrusters on a spacecraft.

1.2 Overall Experimental/Numerical Research Effort

An accurate description of the expanding flow field is essential to an assessment of the interaction between a thruster plume and the spacecraft itself. In an effort to better understand the physics occurring in small thruster flows, a combined experimental/numerical research program has been underway at NASA Lewis. With the continuous advancement of computing technology, numerical flow simulation has become increasingly desirable, both from economic and scientific standpoints. However, experimental data is crucial to the development of any numerical work, and this is especially true for the case of an expanding, rarefied flow. Thus, the overall goal of the program is to advance the theoretical predictions of small rocket expansions to vacuum

conditions through comparison with experimental data.

A reference problem was established through both experimental and numerical considerations. From an experimental standpoint, the thruster was to be as large as possible to minimize the probe size relative to the nozzle. At the same time, the flow field was to maintain similarity with actual (smaller scale) thruster flows. This was insured by requiring that the throat Reynolds number be typical of an actual low-thrust rocket. As documented by Yoshida *et al.* [2], throat Reynolds numbers of high-performance resistojets are typically near 1000. The throat Reynolds number is defined as

$$Re_t = \frac{4\dot{m}}{D_t \mu_0} \tag{1-1}$$

where $\dot{m}$ is the mass flow rate, D_t the nozzle throat diameter, and μ_0 the viscosity of the propellant at the stagnation temperature. According to Manzella [3], the test-cell pressure should be lower than 10^{-4} torr (1.33×10^{-2} Pa) to simulate space conditions. Thus, given the stagnation temperature and hence the stagnation viscosity of a typical propellant, the size of the nozzle was limited by the pumping capability of the facility through the mass flow rate constraint. The nozzle was chosen to be a 100:1 area ratio conical nozzle with an exit plane diameter of 31.8 mm. The conical shape was chosen for the machining and numerical modeling simplicity, plus the fact that conical nozzles are typically used on small thrusters.

There has been experimental data recorded for the expanding flows of small rockets, for example by Bailey [4,5,6] and Legge [7], but in all cases there were inherent difficulties with the numerical modeling of the experimental configurations used. This research effort is the first time that the experimental apparatus was designed specifically for the purpose of advancement of the available numerical codes. As such, it was insured that the reference problem was one that would present no unnecessary complexities to the numerical analyses.

Phase I of the research effort took place in 1990 and involved the flow of carbon dioxide [8]. Pitot pressures and local flow angle measurements were recorded at the exit plane and in the near-field plume of the expanding flow. The flow field was predicted with two numerical techniques, one being a continuum code and the other a particle-level code. The continuum analysis was provided through a solution of the Navier-Stokes equations by the Viscous Nozzle Analysis Program (VNAP) [9]. The second code used the direct simulation Monte Carlo (DSMC) method [10] which models the gas at the molecular level. The main purpose of this phase was to verify that the numerically intensive DSMC technique could be readily applied to an expanding flow typical of small rockets. This was done using a DSMC code which was structured for optimum use on modern supercomputer vectorized hardware. The solutions obtained using the two numerical techniques differed, particularly in the region close to the nozzle lip, with the DSMC results agreeing best with the experimental data.

Phase II of the research program began in June of 1990 and involved the use of nitrogen and argon as propellants in order to both remove the numerical ambiguity of specifying an effective specific heat for carbon dioxide, and also to try to eliminate the experimental hindrance of accumulating black, sooty deposits in the heat exchanger. The author was involved with the experimental aspect of this phase of the program. Pitot pressure and local flow angle measurements were performed for the purpose of further comparison with the two numerical techniques. Both of these measured quantities were easily obtainable from numerical solutions via simple manipulation of the results, as is discussed in detail in Reference 11. The results of the comparisons of the two numerical techniques have been given in detail [11,12,13], and basically established that the continuum code with a no-slip boundary condition at the nozzle wall was not able to predict the rapidly expanding, low-density flow nearly as well as the DSMC code. Another difficulty with the continuum code was using extrapolation for the subsonic portion of the outflow surface which did not model correctly the expansion of the flow into

the vacuum. Thus, the focus of the development of the numerical predictions has recently shifted mainly to the DSMC technique since it exhibits the most promise for providing realistic solutions in the rarefied plume.

1.3 Contents of This Work

The work contained herein pertains mainly to the experimental aspect of the effort, with only a few examples of the latest comparisons made between the DSMC predictions and the experimental results. This thesis is an attempt by the experimentalist to document some of the details of the experimentation that have not yet appeared in the literature. Such details include a complete presentation of all data taken-to-date and an uncertainty analysis for the data. Due to the nature of the experiments, the uncertainty of the results was different for each and every data point. Thus, a general approach to estimating the uncertainty in the data is outlined herein, and example calculations are given for two flow field locations which represent where the highest and lowest flow field gradients of Pitot pressure and local flow angle occurred.

All of the data taken in this study were at the nozzle exit plane or in the forward portion of the plume since the instrumentation used in the current study was not sensitive enough to perform experiments in or near the backflux region. Again, the two quantities measured in the present study were Pitot pressures and local flow angles, and the data were taken over a much larger portion of the forward plume than had been surveyed in Phase I.

Variations in the experimental configuration consisted of two thrusters, two sets of positioning tables, two propellants, and five measurement probes. These variations were divided into seven different classes, hereafter called Cases. Data within a given Case had a uniform operating condition and hardware. These Cases resulted from a progressive effort to obtain more accurate experimental data and/or to try new experimental techniques.

CHAPTER II
Experimental Facility and Hardware

2.1 Vacuum Tank

All experiments described in this work were performed in Tank 5 of the Electric Propulsion Laboratory at the NASA Lewis Research Center in Cleveland, Ohio. The tank is cylindrical, with a diameter of 4.9 m and a length of 19 m. The experiments were actually performed in a smaller cylindrical attachment, called a spool, which has a diameter of 0.9 m and a length of 1.6 m. The pumping capability was provided by twenty 0.8 m oil-diffusion pumps in series with four lobe blowers and four rotating-piston roughing pumps in parallel. A more detailed description of the test facility is given by Finke [14].

For no flow and full pumping capacity, the tank pressure could be maintained near 10^{-4} Pa. However, the cell pressure increased appreciably for small propellant flow rates into the tank. For the Phase II tests it was desired to use the same nozzle as for the Phase I tests, so D_t was fixed at 3.18 mm. Also, due to previous problems where the cartridge heater in the thruster burned out, a lower stagnation temperature of 700 K was decided upon for the Phase II tests. Using the corresponding stagnation viscosity, μ_0, of nitrogen, it was found (by using Eq. (1-1) to compute the mass flow rate) that the mass flow rate necessary for a throat Reynolds number of 1000 caused cell pressures well above the 1.33 x 10^{-2} Pa recommended by Manzella [3] for space-simulation tests. Thus, a compromise was made to use a mass flow rate of nitrogen of 0.068 g/s, which resulted in a throat Reynolds number of 850 and a cell pressure of about 3 x 10^{-2} Pa, which was thought to be close enough to Manzella's suggested value.

2.2 Simulated Thrusters

The thrusters used were not actual space-quality hardware. They were simulated thrusters, designed simply to generate expanding flows typical of resistojets. Two different heat exchanger designs were used, but the nozzles for both thrusters were designed from the same specifications. A diagram of the nozzle is shown below in Figure 2-1. The labels T_m and T_e are included to indicate the position where two thermocouples were located to monitor the nozzle temperature profile. The values of all of the dimensions shown in Figure 2-1 are given in Table 2-1. Again, this nozzle design was used for both of the thrusters utilized in the current work.

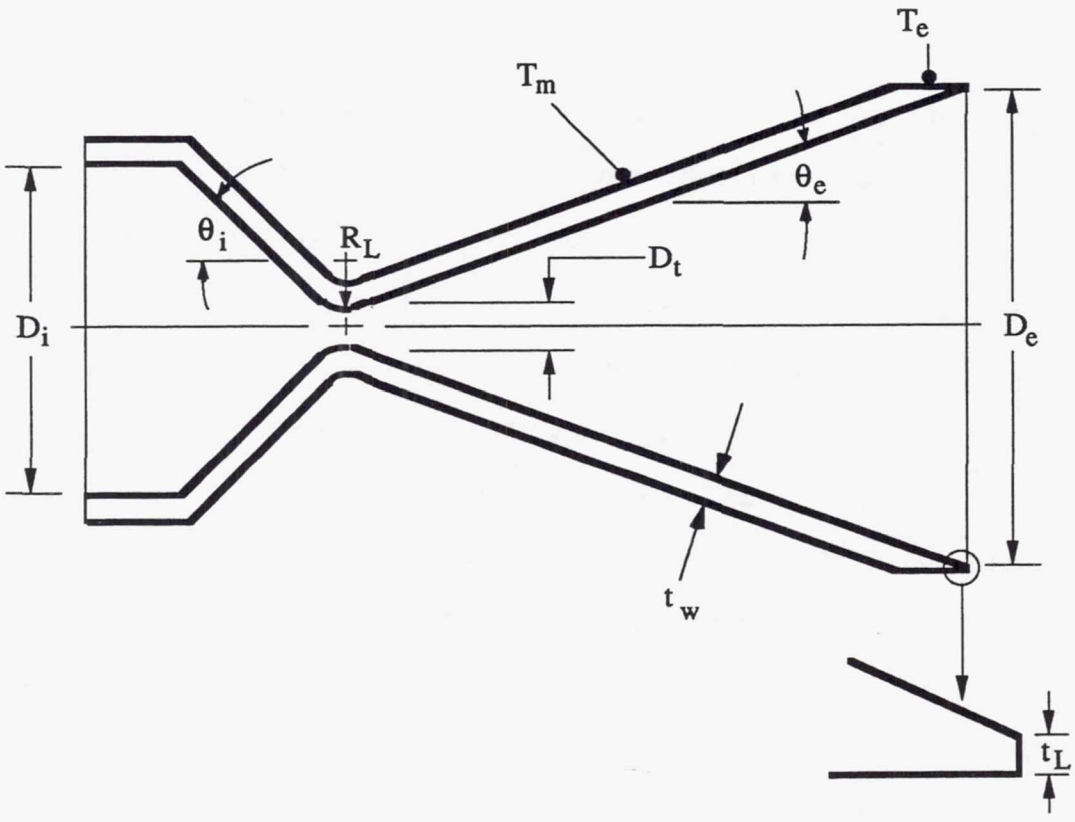

Figure 2-1. Nozzle geometry and thermocouple locations.

Table 2-1. Nozzle geometry information.

Inlet diameter, D_i	22.1 mm
Throat diameter, D_t	3.18 mm
Exit diameter, D_e	31.8 mm
Inlet half-angle, θ_i	45°
Exit half-angle, θ_e	20°
Longitudinal radius, R_L	3.18 mm
Wall thickness, t_w	1.65 mm
Lip thickness, t_L	0.25 mm
Area ratio, $(D_e/D_t)^2$	100

The first thruster, hereafter called thruster 1, heated the propellant by flowing the gas through a 3.2 mm diameter tube which was coiled around a cylindrical cartridge heater. The entire heat-exchanger section was wrapped with foil to minimize the radiation losses. However, there was a very small contact area between the coiled tube and the heater, and there was no other conducting media present during operation due to the vacuum surroundings. Because of this inefficient heat exchanger design, the heating element was operated at unnecessarily high temperatures for a given desired gas temperature. Consequently, there were problems with burning out of the heater during a run, as mentioned in the previous section. Also, the thruster was mounted at the rear, which meant that thermal expansion of the entire thruster caused the thruster exit plane to move in the direction of flow from its original unheated position. For both of these reasons, a more efficient heat exchanger design was pursued.

The improved thruster, hereafter called thruster 2, allowed the gas to flow through an annular passage, which put the propellant in direct contact with the heater surface. The cross-sectional view of thruster 2 is shown in Figure 2-2. The white region shows the propellant path through the thruster. With the new thruster, roughly fifteen percent less power was needed to produce the same gas temperature for a given mass flow rate. Correspondingly, the nozzle temperatures T_m and T_e were significantly lower for thruster

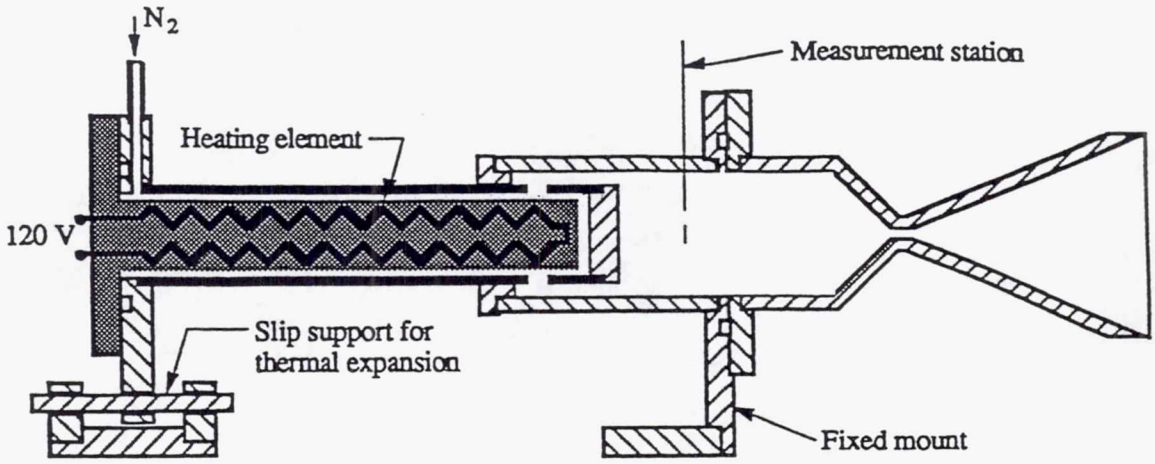

Figure 2-2. Cross-sectional schematic of thruster 2.

2, compared to those for thruster 1. Thruster 2 was mounted at the nozzle end, with most thermal expansion serving to move the thruster body, which was mounted on a sliding mechanism, rather than the nozzle. Also, the nozzle was fabricated separately and attached to the thruster body with a bolted flange and sealed with a metallic O ring to allow ease in changing nozzles for future experiments.

2.3 Probes

Two types of probes were used in the experiments. Pitot probes were used to measure both Pitot pressure and local flow angle. Conical probes were also used to measure local flow angle. Variations of each probe type were used, the details of which are described below.

A schematic of a typical Pitot tube that was used is shown in Figure 2-3. Three different sizes of Pitot tubes were used, with the significant dimensions given in the figure. The Pitot tube is a simple device which measures the stagnation pressure of a gas at a point in the flow. If the local flow is subsonic, the pressure measured is the actual stagnation pressure of the gas. If the local flow is supersonic, the Pitot pressure is the stagnation pressure behind the shock induced by the probe.

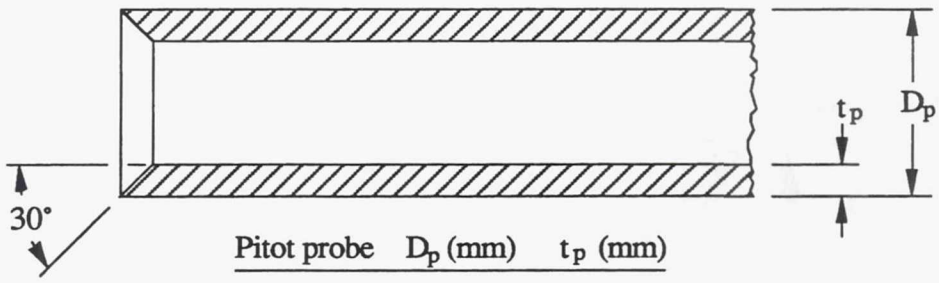

Pitot probe	D_p (mm)	t_p (mm)
1	1.63	0.15
2	1.02	0.15
3	6.35	0.81

Figure 2-3. Cross-sectional view of typical Pitot tube and relevant dimensions.

The Pitot pressure mentioned above is actually the measured pressure when the probe is aligned with the local flow. Following the experimental procedure of Bailey [6], the local flow angle was established by rotating the Pitot tube at a point in the flow until the pressure reading was a maximum. So, Pitot pressures and local flow angles were measured simultaneously with the Pitot tube.

An alternate way of measuring the local flow angle was to use a probe with a conical tip and attempt to balance the flow over the cone. This balancing in the present work was performed by using probes with static pressure taps spaced at 180 degrees on the cone surface and rotating the probe until the pressures balanced. Two variations of the conical probe, conical probe 1 and conical probe 2, were used for measuring flow angles. Conical probe 1 was a commercially available United Sensor probe which had a total pressure tap and four static pressure taps spaced at 90 degrees on the cone surface. For the present study only two opposed static taps were utilized. The lines from these two taps are shaded in Figure 2-4, which shows this probe.

Since only two static pressure taps were needed to measure flow angles, rather than four static taps and a total tap, another conical probe was fabricated at NASA Lewis and designated conical probe 2. A cross-sectional view of this probe is shown in Figure 2-5.

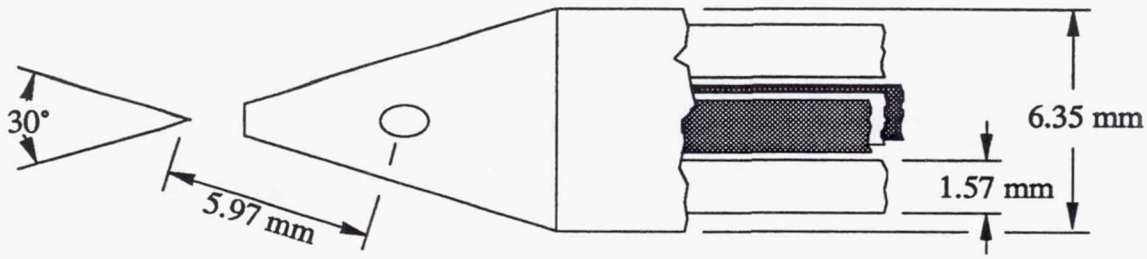

Figure 2-4. Conical probe 1.

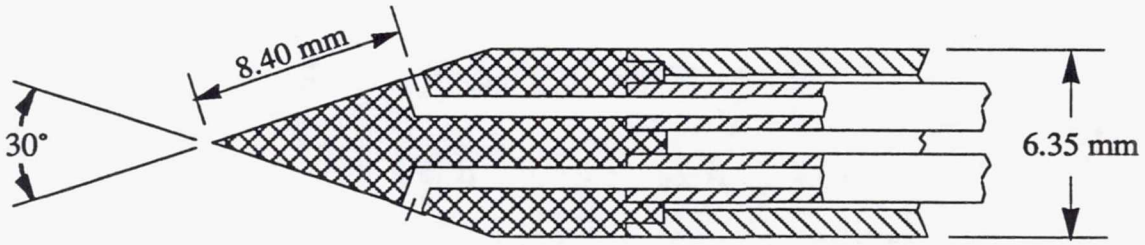

Figure 2-5. Cross-sectional view of conical probe 2.

2.4 Positioning Tables

The flow from a conical nozzle expanding to virtually vacuum surroundings can be assumed axially-symmetric, and the symmetry was verified to within experimental uncertainty for both of the nozzles by initially taking data across the entire exit plane. Thus, data was only needed in one plane containing the nozzle centerline to study a given flow field. The horizontal plane was chosen, due to the convenience in positioning the traversing tables. The coordinate system adopted had one axis (Z) on the nozzle centerline and the other axis (R) perpendicular to the Z-axis. The origin of this R,Z coordinate system was at the center of the nozzle-exit plane. So that the reader can more easily envision the probe position relative to the nozzle, most of the positions are referred to by the dimensionless coordinates $\overline{R}$ and $\overline{Z}$, where

$$\overline{R} = \frac{R}{D_e} \quad ; \quad \overline{Z} = \frac{Z}{D_e} \tag{2-1}$$

There were two sets of positioning tables used to move the probes. The forward-plume travel capabilities of both table sets are illustrated in Figure 2-6. The first table set, hereafter called Table Set 1, consisted of four hand-operated Daedal tables, situated with the rotary table mounted atop three orthogonal translational tables. This set had very limited translational travel, and the corresponding experimental region extended 24 mm radially (R) and 36 mm axially (Z) from the center of the nozzle-exit plane. The majority of the experiments were done in the Table Set 1 region. The probe position was monitored by Schaevitz linear-variable-differential transformers (LVDTs).

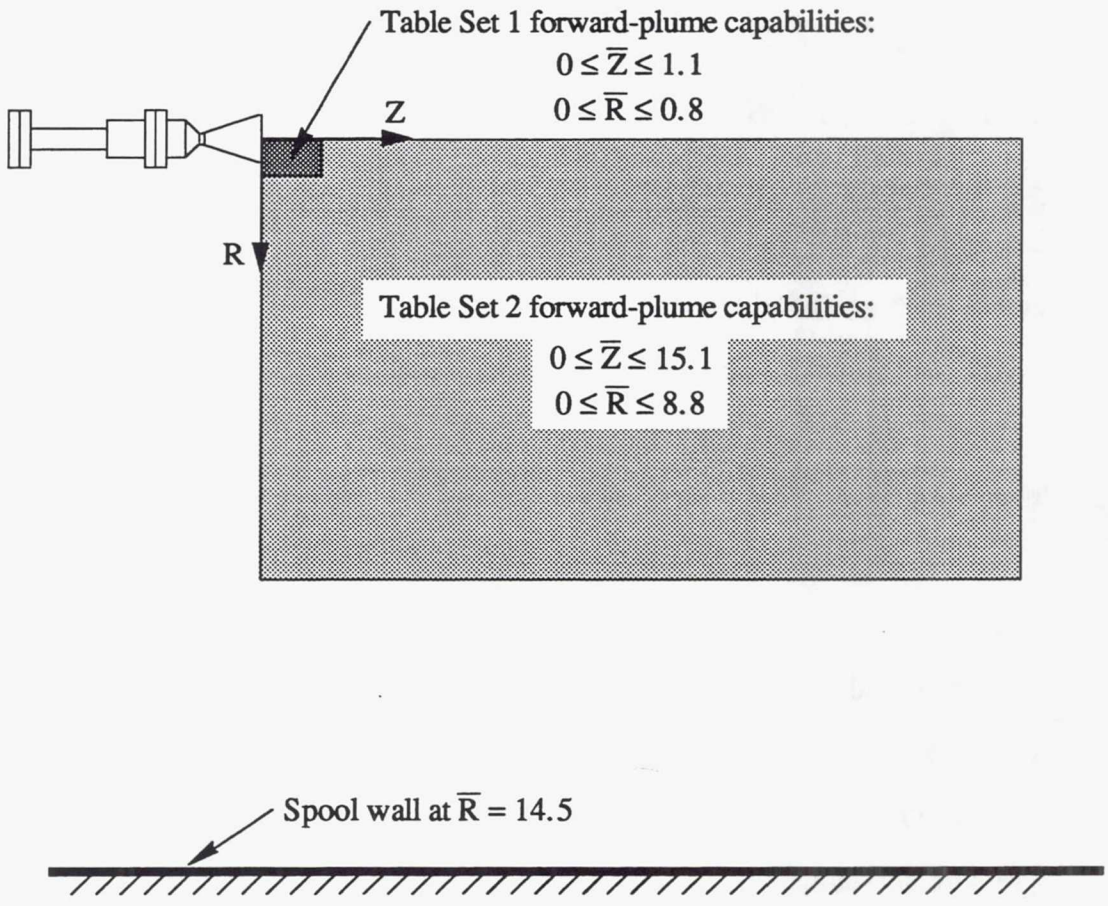

Figure 2-6. Forward-plume travel capabilities of both table sets.

The second set, hereafter called Table Set 2, was a Compumotor 4000 stepping-motor-driven set with a rotary table mounted atop two perpendicular translational tables. Table Set 2 provided an experimental region extending 280 mm radially and 480 mm axially from the center of the nozzle-exit plane. Table Set 2 greatly increased the speed of moving the probe with a control panel allowing variable speed and easy positioning. The probe position was monitored by encoders mounted on each table.

2.5 Measuring Devices

To monitor the operating parameters of the thruster, the stagnation pressure, stagnation temperature, nozzle surface temperatures, and mass flow rate were measured. The stagnation quantities were measured upstream of the nozzle throat in a 22.1 mm diameter section, which is illustrated in Figure 2-2. The stagnation pressure was measured with a Vacuum General capacitance manometer having a full scale of 13.3 kPa, a three decade measurement range, and a listed manufacturer's accuracy of 1.0 percent of reading. The gas stagnation temperature was measured with a half-shielded, chromel-alumel thermocouple with the hot junction located at the centerline of the measurement section and connected to a digital voltmeter with self-contained cold-junction compensation. The nozzle temperatures were measured by two chromel-alumel thermocouples that were tack-welded to the outer wall surface. The accuracy of the thermocouples was estimated to be within ± 2.5 K.

The propellant flow rate was measured with a Teledyne Hastings-Radist mass-flow transducer that related thermal changes in a capillary tube to mass flow rate. The flow rate was controlled by a UNIT Instruments mass-flow controller consisting of a similar flow meter and a feedback loop to an electrically operated valve. The flow meter and controller were calibrated for nitrogen and argon using a calibration tank of known volume with pressure and temperature gauges. The tank was equipped with an automatic valve that allowed flow for exactly two minutes. Given the initial and final pressure and temperature

and the molecular weight of the gas, the mass flow rate into the tank could be calculated. The flow meter readings had a better linear correspondence to the actual (calibration tank) flow rates than the flow controller readings, so the flow meter reading was used. That is, the flow controller was only used to obtain the desired flow meter reading. Based on the repeatability of this test, it was felt that the test flow rates were within ± 3 percent of the desired flow rate of 0.068 grams per second for all runs performed.

The tank pressure was measured with Veeco Instruments ionization gages placed at three different locations in the tank. The pressures measured on all three of these were usually about the same. The tank pressure, P_b, refers to the average of these three readings. The Pitot and cone static pressures were all measured with Vacuum General capacitance manometers. For the regions in close to the nozzle, a manometer with a full scale of 1.33 kPa, a three decade measurement range, and a listed accuracy of 1.0 percent of reading was used. The far-field Pitot pressure measurements were taken using a manometer with a full scale of 133 Pa, a three decade measurement range, and a listed accuracy of 0.25 percent of reading. Two 133 Pa full-scale manometers were used to measure the cone static pressures for all flow angle measurements.

CHAPTER III
Experimental Procedure and Related Uncertainty

Figure 3-1 below shows the experimental configuration used for the testing. The traverse tables were positioned below the forward-plume of the thruster with the probe mounted on top, as shown in the figure. The entire experimental apparatus was mounted on a mobile cart with a flange that mated with the flange on the spool chamber. The seal between the test-cart flange and the spool flange was made with a rubber O ring.

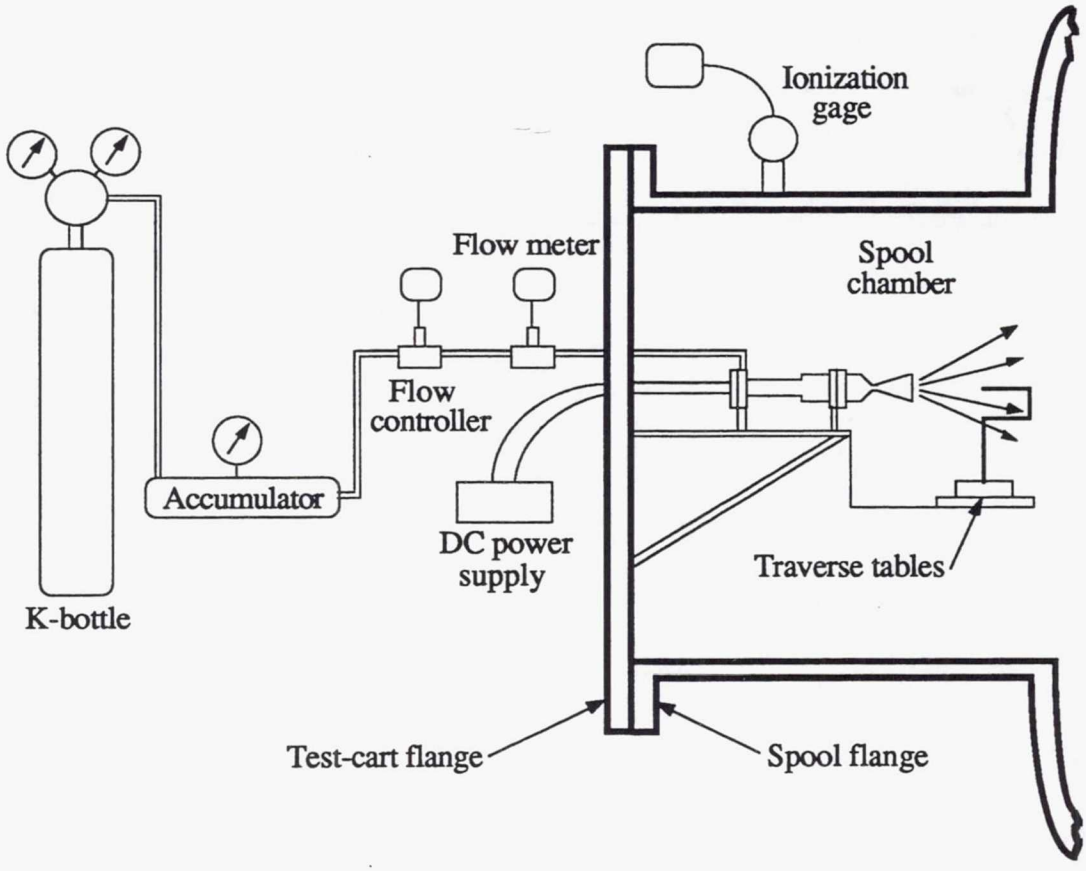

Figure 3-1. Schematic diagram of the experimental configuration.

3.1 Start-Up Process

Before the apparatus was put into the vacuum chamber, the probe was positioned at the origin of the R,Z coordinate system shown in Figure 2-6 in the previous chapter. This position was established by placing the probe tip at the center of the nozzle exit plane with the aid of a steel scale and the traverse tables. The uncertainty in this process was less than ± 0.5 mm in both the radial and axial directions.

The apparatus was then inserted into the vacuum facility and the flanges were held together with C clamps. Next, the valve (not shown in Figure 2-6) between the main vacuum tank and the spool containing the experimental apparatus was opened, and the spool evacuated until the pressure was about 10^{-4} Pa. At that point all capacitance manometers were zeroed. The mass flow rate was then established by adjusting the flow controller until the desired flow meter reading was attained. Immediately after the flow was established, the DC power supply was turned-on to energize the cartridge heater within the thruster. The voltage was first set to a value higher than the value known to be needed at steady-state conditions. By "known" value it is implied that the wattage required to produce the 700 K stagnation temperature was very repeatable from test to test. This procedure was done to expedite the heat-up process. As the stagnation temperature of the gas approached the desired value, the voltage was lowered to the known steady-state value. When all thruster and nozzle temperature readings reached steady state, the zero angle of probe rotation had to be determined.

The zero reference position for the probe rotation angle, θ, was found by rotating the probe, while located at the zero R,Z position, until it was aligned with the local flow. This procedure was chosen over visually-aided positioning because the nozzle centerline is not a tangible entity, which made it impossible to be sure that the probe was indeed at exactly zero rotation. The uncertainty in establishment of the rotation reference position differed for the different probes used, and this is discussed in more detail in the following section. The entire start-up process usually took about 90 minutes.

3.2 Data Acquisition

The data was always taken as a radial scan at a fixed axial location or as an axial scan at a fixed radial location. The probe was moved from point to point by remote control using the traversing table set. There were two particular methods used to obtain data at a given point, which corresponded to the two different types of probes used. These methods are explained in the subsections below.

3.2.1 Pitot Probe

One may obtain both maximum Pitot pressure and flow angle data using only a Pitot probe. As mentioned earlier, the Pitot pressure for a given probe tip location is a maximum when the probe is aligned with the local flow. Thus, by rotating the probe at each measurement location, one may record the local flow angle and the corresponding Pitot pressure using this fact.

A typical plot of Pitot pressure versus probe angle is shown in Figure 3-2.

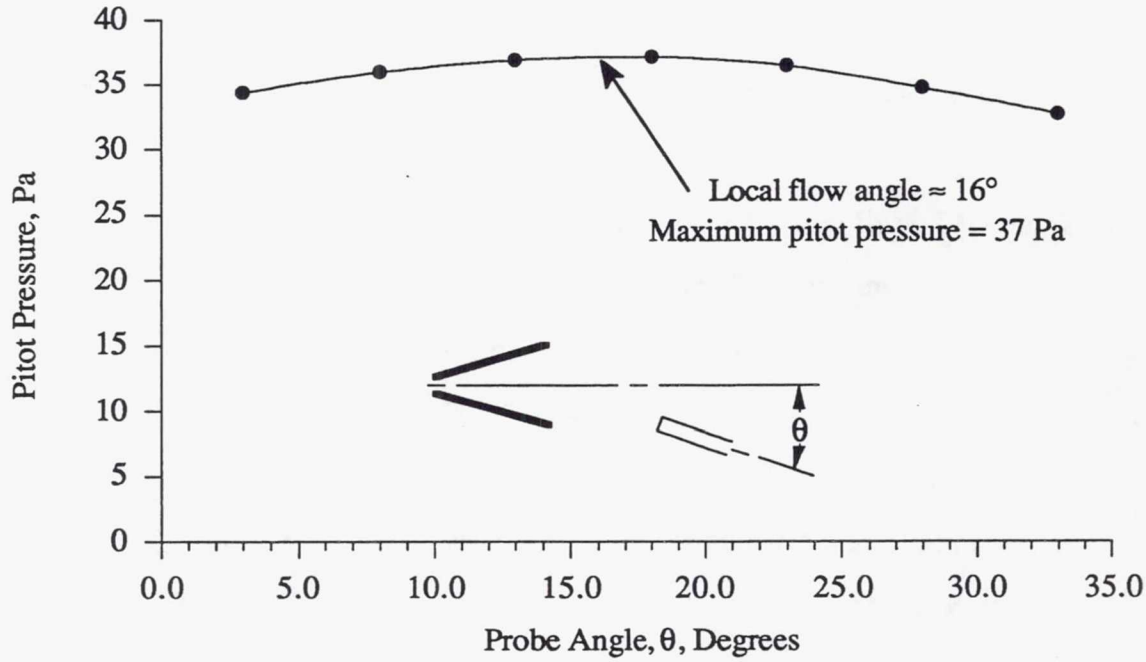

Figure 3-2. Pitot probe rotation at $\overline{R} = 0.38$ and $\overline{Z} = 0.76$.

As can be seen by observing the ordinate in the above plot, this method did not produce sharply defined maximum pressures. The lack of resolution in determining a clear maximum caused a flow angle uncertainty of about ±2 degrees, which was fairly uniform over the entire experimental region. The Pitot pressure uncertainty associated with this measurement technique was solely due to the manometer uncertainty.

The average time required for a Pitot probe 2 pressure reading to stabilize, i.e., the response time, was around 3 minutes. As such, it took about 20 minutes per R,Z location to measure the flow angle and the corresponding maximum Pitot pressure. Thus, about 18 locations could be measured per test day. The corresponding average response times for Pitot probes 1 and 3 were about 1 minute and 5 seconds, respectively.

3.2.2 Conical Probe/Pitot Probe

This experimental technique involved measuring the local flow angles and maximum Pitot pressures separately. A conical probe was first used to measure the flow angles. With these angles known, the Pitot tube rotation was not required, as the probe could be immediately aligned with the measured flow angles.

As mentioned in the previous chapter, both of the conical probes had static pressure taps on opposite sides of the cone, which were located in the experimental (horizontal) plane. As the probe was rotated at a point in the flow, the two cone static pressures would become equal at some angle of rotation. Assuming that the finite spacing of the pressure taps was small enough to keep the local pressure gradients of the flow field from affecting the measurement, and also that the probe itself did not significantly alter the local flow, this angle of rotation could be, and was, interpreted as the local flow angle. However, as is further discussed in Chapter IV, there was strong evidence that these factors did affect the measurements in varying degree depending on the position in the plume.

A typical data set from a rotary scan of conical probe 2 is shown in Figure 3-3. The conical probe flow angle measurements generally produced sharp pressure crossovers,

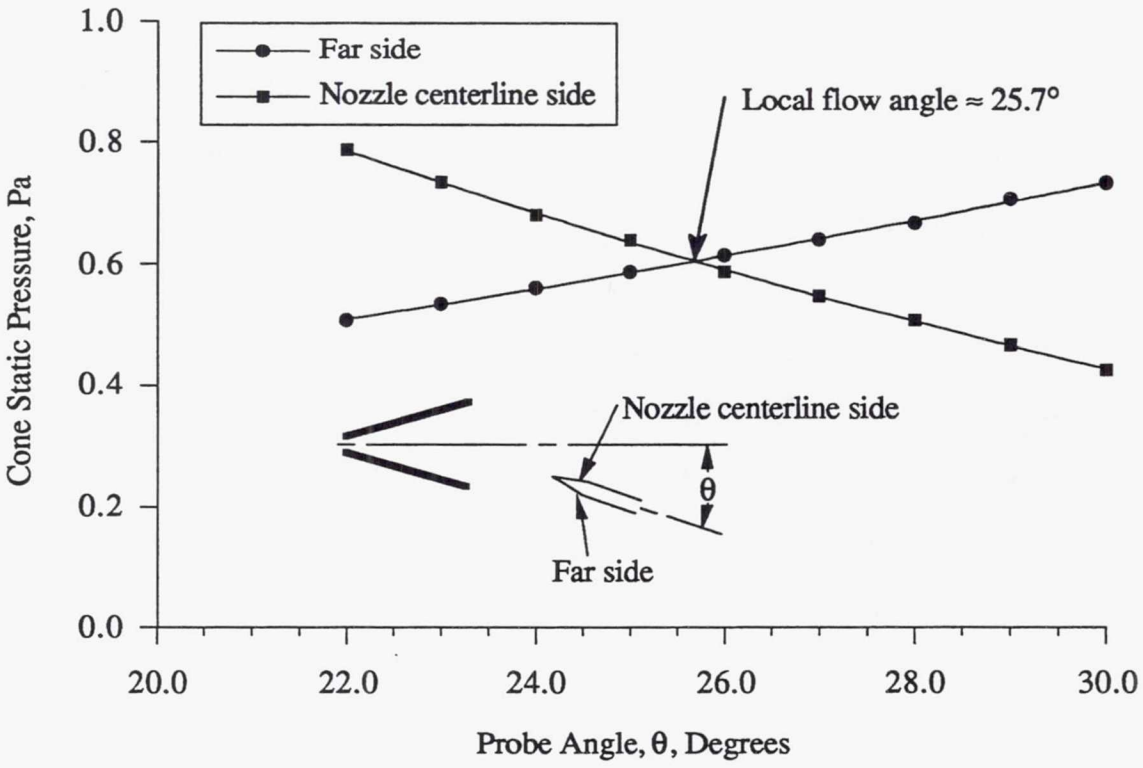

Figure 3-3. Conical probe rotation at $\overline{R} = 0.94$ and $\overline{Z} = 1.89$.

which occurred over a much smaller range of rotation than needed for the Pitot probes. As such, the resolution of the local flow angle measurements was greatly increased with the conical probe. This resolution (in determining the crossover point) was within ± 0.5 degrees for the far-field plume regions where the cone static pressures were the lowest, and decreased to nearly zero near the R,Z coordinate origin. After measuring the flow angles, the Pitot pressures were measured by positioning the Pitot tube at the known flow angles. Again, due to the very weak dependence of Pitot pressure on flow angle, there was no appreciable uncertainty in the Pitot pressure measurements other than that due to the manometer and position uncertainties.

The response time, i.e., the time required for the pressure reading to stabilize for a given probe position, was similar to that of Pitot probe 2 since the tubing for both of the conical probes was on the order of 1 mm in diameter. However, since the conical probe

flow angle technique was based on the relative pressures of the two taps rather than an absolute pressure, the probe could be rotated in the proper direction (to bring the two pressures closer together) long before the pressure readings stabilized completely. It was only necessary to allow the pressure readings to attain steady state as the probe rotation angle neared the local flow angle. Usually some fine tuning was required at the end, but typically the total time required for a flow angle measurement was about 5 minutes. In addition, a time equal to the Pitot response time was then needed for the Pitot pressure reading (during a different day of testing) to be taken. Thus, the total time needed to measure both quantities was between 5 to 8 minutes per location for this technique.

3.3 Cool-Down Process

After the experimentation was finished, the thruster was cooled down before being removed from the vacuum chamber. This process consisted of turning off the power to the heater and allowing gas to continue to flow through the thruster. It was important to leave the flow on to increase the cooling rate because, with virtually perfect vacuum surroundings, radiation was the only other significant mode of energy transfer from the thruster. Generally, it took about 45 minutes until the maximum thruster surface temperature was below 400 K, at which time the flow was turned off and the remainder of the energy was lost by radiation. Thus, a total of about 135 minutes was required for the start-up and cool-down processes for a day of experimentation.

3.4 Uncertainty Analysis

In the analysis presented herein, there were three steps to approximating the uncertainty in an experimental value. The first step was to attempt to identify all significant sources of potential error for a given measurement. The second was to try to quantify the uncertainty due to each source separately. Adding the contributions to get an overall potential error range for the measurement was the final step in the analysis.

For the current example, the results for the flow of nitrogen were used because extensive tests were done using both Pitot probes and conical probes for nitrogen, whereas for argon only limited Pitot probe tests were conducted. Two flow field locations were chosen which represented the approximate locations of the highest and lowest flow field gradients of pressure and flow angle. The approximate location of the highest gradients, hereafter called location 1, was at the nozzle exit plane and slightly off the nozzle centerline ($\overline{R} = 0.19$, $\overline{Z} = 0$). On the other extreme, at $\overline{R} = 1.89$, $\overline{Z} = 5.04$, the measurement location furthest from the R,Z coordinate origin, the local gradients were extremely low. This location is hereafter referred to as location 2.

At the axial location $\overline{Z} = 0$ for the flow of nitrogen, there were various probes used to make radial scans to measure the flow field properties. For example, Pitot probes 1 and 2 were used to measure the Pitot pressures and Pitot probes 1 and 2 and conical probe 1 were all used to measure the local flow angles. All of these results appear in the following chapter. For convenience, the uncertainty analysis was performed only on the Pitot probe 2 (Pitot pressure and flow angle measured) and conical probe 1 (flow angle measured) results. At the axial location $\overline{Z} = 5.04$, Pitot probe 3 (Pitot pressure measured) and conical probe 2 (flow angle measured) were used, and the uncertainty analysis was performed for these results as well.

The approach given here was used to estimate the experimental uncertainty of Pitot pressure and/or local flow angle data. The experimental data which were needed to use the following technique were simply measurements of maximum Pitot pressure, local flow angle, and cone static pressure (if a conical probe was used to measure flow angle) at a matrix of flow field locations. Using these values, the local derivatives of the measured properties with respect to R and Z were approximated as finite differences.

3.4.1 Pitot Pressure Measurements

The uncertainty in the Pitot pressure data depended on the local gradient of Pitot

pressure and the Pitot pressure itself. The local gradient of Pitot pressure determined the measurement uncertainty associated with the ±0.5 mm radial and axial probe position uncertainty. This uncertainty was due entirely to the error in initially positioning the probe at the R,Z coordinate origin. That is, both of the table sets used were accurate enough that the incremental uncertainty associated with moving the probe relative to the origin was negligible compared to ±0.5 mm. The Pitot pressure reading at a given location dictated the uncertainty involved with the manometer reading. As stated in the previous chapter, the uncertainties for all of the capacitance manometers were given as a percent of the reading.

The Pitot pressure uncertainties associated with probe position inexactness were computed separately for the radial and axial directions. Using the Pitot pressure measurements around a particular location, the local derivatives of Pitot pressure with respect to R and Z were approximated using finite differences. Central differences were used whenever possible, and one-sided differences were used otherwise. Then, the derivatives in both directions were multiplied by ±0.5 mm to get the corresponding Pitot pressure uncertainties due to position inexactness. For location 1, the magnitudes of the local radial and axial derivatives of Pitot pressure were about 30 and 6 Pa/mm, respectively. Thus, ±0.5 mm radial and axial position shifts corresponded to Pitot pressure changes of about ±15 Pa and ±3 Pa. Due to the much smaller Pitot pressure derivatives at location 2, the Pitot pressure changes associated with ±0.5 mm radial and axial position shifts were a mere ±0.04 Pa and ±0.003 Pa, respectively.

For location 1, the Pitot pressure reading of 231 Pa was measured using a 1.33 kPa full-scale capacitance manometer, which had a listed manufacturer's accuracy of 1 percent of reading. Thus, the uncertainty associated with the manometer reading was roughly ±2 Pa. The 2.67 Pa Pitot pressure measurement at location 2 was obtained using a 133 Pa full-scale capacitance manometer with a listed accuracy of 0.25 percent of reading. The manometer thus contributed ±0.007 Pa to the uncertainty in the measurement

at location 2. Table 3-1 at the end of this section contains all of the Pitot pressure uncertainty components and the corresponding total uncertainties for locations 1 and 2. The ±20 Pa and ±0.05 Pa uncertainties constituted approximately 9 and 2 percent of the Pitot pressures measured at locations 1 and 2, respectively.

The uncertainties in Table 3-1 are given such that one takes the measured value and adds on and subtracts off the amounts which appear in the total uncertainty row to get the range which contains the actual value. For example, at location 1 the actual Pitot pressure was estimated to be between 211 and 251 Pa (231 Pa ± 20 Pa).

3.4.2 Flow Angle Measurements with a Pitot Probe

The uncertainty in the flow angle data obtained with a Pitot probe was considered to depend only on the local derivatives of flow angle with respect to R and Z. Again, the local derivatives were used to compute the uncertainty in the data involved with the probe position inexactness. Also, for the Pitot probe there was a ±2 degree potential error associated with the resolution of the pressure maximum, as was discussed above. It was assumed that the stream pressure and the error in the capacitance manometer reading did not change over the relatively short time it took to perform a single probe rotation, and hence that the Pitot pressure uncertainty did not enter into flow angle uncertainty.

As mentioned above, uncertainty analyses were performed for the Pitot probe 2 and conical probe 1 flow angle measurements at location 1. The error in the conical probe measurement is discussed in the following subsection. The flow angle uncertainties at location 1 corresponding to ±0.5 mm radial and axial position shifts were about ±2.0 degrees and ±0.3 degree, respectively. These values constituted averages of calculations done using the local flow angle data from both Pitot tube 2 and conical probe 1, and they were used for both the Pitot probe and conical probe flow angle error analyses.

The components of the flow angle uncertainty analyses and the corresponding totals appear in Table 3-2 at the end of the section. The errors are presented in the same

form as those in Table 3-1. Notice that the information for both the Pitot probe and conical probe flow angle uncertainty evaluations appears in Table 3-2, with the total uncertainties given in two different rows.

3.4.3 Flow Angle Measurements with a Conical Probe

The total uncertainty in the flow angle data obtained with a conical probe was considered to depend on several factors. First, the local derivatives of flow angle with respect to R and Z were needed to evaluate the error associated with position inexactness. Also, there was a potential error associated with the resolution of the flow angle, as discussed above. For the conical probe there was the additional uncertainty caused by the finite pressure tap spacing in a flow field with appreciable static pressure gradients in some locations. One additional source of uncertainty in the conical probe flow angle measurements would have been the uncertainties in the two manometer readings. Initially, there were problems with manometer zero shift (often in opposite directions) with time during a run. This would have obviously resulted in significant errors since the method relied on balancing the two pressure readings. To alleviate this problem, the manometers were re-zeroed periodically throughout each run to insure that manometer drift was kept small and the incremental uncertainty negligible. The re-zeroing was usually done about every 90 minutes.

As mentioned in the previous subsection, at location 1 there were flow angle uncertainties of about ± 2.0 degrees and ± 0.3 degrees for respective ± 0.5 mm radial and axial position uncertainties. The pressure crossover at location 1 was so distinct that the uncertainty associated with the resolution could be neglected. For conical probe 1 there was a spacing of 3.1 mm between the two static pressure taps. At location 1 the derivative of cone static pressure with respect to R was about - 3 Pa/mm, so there was approximately a 9 Pa static pressure drop across the taps, with the nozzle centerline side being higher. Thus, the probe had to be rotated to a larger angle than the actual flow angle to balance the

cone static pressures. According to a plot similar to Figure 3-3, the error induced by this phenomena was near - 3.5 degrees. However, this error was by no means exact and was thus given a final error of - 3.5 ± 1.5 degrees, which means that the flow angle measurement made at location 1 was between 2 and 5 degrees too high from this effect. With all sources of error considered, the flow angle measurement made at location 1 with conical probe 1 had an uncertainty of - 3.5 ± 3.8 degrees. Thus, following the error presentation convention described above, the actual flow angle was approximated to be somewhere between the measured value + 0.3 degrees and the measured value - 7.3 degrees (between 12.6 and 5.0 degrees).

At location 2 only conical probe 2 was used to measure the local flow angle, and the flow angle uncertainties corresponding to ± 0.5 mm radial and axial position shifts were ± 0.17 degrees and ± 0.03 degrees, respectively. The resolution problem associated with the pressure crossover at location 2 added another ± 0.5 degrees uncertainty to the measured angles. Also, a comparison of the pressure drop across the static tap spacing at location 2 with the pressure-crossover profile showed that there was negligible flow angle error caused by that phenomena. Incidentally, conical probe 2 had a pressure tap spacing of 4.3 mm, which caused the static-pressure-related errors to be even larger than for conical probe 1. This is discussed further in the next chapter.

Table 3-1. Pitot pressure uncertainty breakdown for the two selected locations.

	uncertainty in Pitot pressure measurement at $\overline{R} = 0.19, \overline{Z} = 0$ (Pa)	uncertainty in Pitot pressure measurement at $\overline{R} = 1.89, \overline{Z} = 5.04$ (Pa)
uncertainty due to ± 0.5 mm inexactness in R	± 15	± 0.04
uncertainty due to ± 0.5 mm inexactness in Z	± 3	± 0.003
uncertainty due to 0 - 1330 Pa capacitance manometer reading	± 2	N/A
uncertainty due to 0 - 133 Pa capacitance manometer reading	N/A	± 0.007
Total uncertainty	**± 20**	**± 0.05**

Table 3-2. Local flow angle uncertainty breakdown for the two selected locations.

	uncertainty in local flow angle measurement at $\overline{R} = 0.189, \overline{Z} = 0$ (Degrees)	uncertainty in local flow angle measurement at $\overline{R} = 1.890, \overline{Z} = 5.039$ (Degrees)
uncertainty due to ± 0.5 mm inexactness in R	± 2.0	± 0.17
uncertainty due to ± 0.5 mm inexactness in Z	± 0.3	± 0.03
uncertainty due to Pitot probe flow angle resolution	± 2.0	N/A
uncertainty due to conical probe flow angle resolution	negligible	± 0.50
error due to static pressure gradients across finite tap spacing for conical probe	-3.5 ± 1.5	negligible
Total uncertainty for Pitot probe	**± 4.3**	N/A
Total uncertainty for conical probe	**-3.5 ± 3.8**	**± 0.70**

CHAPTER IV
Results and Discussion

4.1 Case Definitions

Some of the Cases consisted of data from a single day of testing, while others consisted of data from many days. For each day of testing, certain values were recorded which established the operating condition for the experiment. Table 4-1 below shows the average operating condition for each of the seven Cases. It should be noted that the uncertainty analysis in the last chapter did not account for the uncertainty in operating conditions from day-to-day.

Table 4-1. Average operating conditions for the seven Cases.

Case	$\dot{Q}$ (W)	$\dot{m}$ (kg/s)	P_b (Pa)	P_o (Pa)	T_o (K)	T_m (K)	T_e (K)
1	75.3	6.8×10^{-5}	0.045	6130	698	554	542
2	75.7	6.8×10^{-5}	0.035	6400	697	553	541
3	67.6	6.8×10^{-5}	0.036	4670	648	523	513
4	63.5	6.8×10^{-5}	0.031	6210	700	506	498
5	63.5	6.8×10^{-5}	0.031	6250	700	506	498
6	63.5	6.8×10^{-5}	0.032	6420	700	511	503
7	64.5	6.8×10^{-5}	0.032	6420	700	511	503

The information in the various columns of Table 4-1 is as follows:

$\dot{Q}$ - Power supplied to the cartridge heater.

$\dot{m}$ - Propellant mass flow rate.

P_b - Surrounding vacuum pressure, or back pressure.

P_o - Propellant stagnation pressure.

T_o - Propellant stagnation temperature.

T_m - Nozzle surface temperature half way between the throat and the exit plane.

T_e - Nozzle surface temperature near the exit plane.

A change in the propellant or hardware was what marked a change in the Case number. The propellant and hardware combinations which characterized the various Cases are given below in Table 4-2. Recall that all of the hardware was discussed in Chapter II.

Table 4-2. Propellant and hardware information for the seven Cases.

Case	Propellant	Thruster	Table Set	Probe
1	nitrogen	1	1	Pitot 1
2	nitrogen	1	1	Pitot 2
3	argon	1	1	Pitot 2
4	nitrogen	2	1	Pitot 2
5	nitrogen	2	1	conical 1
6	nitrogen	2	2	conical 2
7	nitrogen	2	2	Pitot 3

4.2 Results

In this section all of the measurements that were taken are presented. As mentioned in Chapter I, the purpose of the overall current research effort was to make extensive comparisons between the experimental and numerical results. However, the comparisons for all of the Table Set 1 data have appeared in the literature [11,12,13]. Those comparisons were not included herein; instead the reader is referred to the corresponding publications. The Table Set 2 data was very recently acquired, so comparisons between

those results and the corresponding DSMC predictions are included herein. The comparisons are given to show the reader the state of the numerical predictive technology. The numerical output was manipulated to attempt to account for the shock induced by the Pitot probe to generate pressure values comparable with the experimental Pitot pressures, and the interested reader can find the details of the procedure in Reference 11. Basically, the output manipulation procedure involved the calculation of the stagnation pressure behind a normal shock and then an additional correction for rarefaction effects.

Even though it would have been a visual convenience for the reader if the experimental data was fit with curves (for each axial location), the author did not want to imply a knowledge of which data trends were and were not physically real. As such, the experimental data are all represented by symbols, and the only curves which appear in the plots in this section represent the predictions of the DSMC numerical technique.

4.2.1 Case 1

The data taken for Case 1 consisted of Pitot pressure and flow angle measurements at four different axial locations: Z = 0, 12, 24, and 36 mm. Figures 4-1 and 4-2 at the end of the section show the measured Pitot pressures and flow angles, respectively. As can be seen in Figure 4-2, there were humps in the flow angle profiles, and a question was raised as to whether they were real or probe-induced. It was felt that using a smaller diameter Pitot probe might disturb the flow field less and remove some of the probe-induced errors in the flow angle measurements. This was the notion which prompted the Case 2 testing.

4.2.2 Case 2

Pitot pressure and flow angle measurements, which are respectively shown in Figures 4-3 and 4-4, were taken for Case 2 also. The smaller diameter Pitot tube was used, and the same axial stations were surveyed as for Case 1. The humps in the flow angle profiles diminished somewhat, which showed that they were at least partially probe

related.

Case 2 was referred to as Configuration 1 in References 11 and 13. Each provided comparisons of the Pitot pressure data with the predictions of both (continuum and DSMC) numerical techniques. The continuum (VNAP) computations were made only up to the nozzle exit plane, so the VNAP results were only presented at the Z = 0 location.

4.2.3 Case 3

It was also desired to create a data base for a monatomic propellant. Since Pitot probe 2 (Case 2) had seemed to produce more reasonable flow angles than the larger Pitot probe 1 (Case 1), Pitot probe 2 was utilized for Case 3. In Case 3 argon was used as the propellant and the same measurements were performed as in Case 2. The Pitot pressure and flow angle measurements at the four axial locations are shown in Figures 4-5 and 4-6, respectively.

4.2.4 Case 4

For this case thruster 2 was used. Again, Pitot pressure and flow angle measurements, which are respectively shown in Figures 4-7 and 4-8, were performed. As in Cases 2 and 3, Pitot probe 2 was used. Since the flow angle data looked very similar to the data obtained in Case 2, flow angles were only recorded at two of the axial stations. The Pitot pressures were recorded at all four axial locations since there were notable differences in the pressure profiles between Cases 2 and 4.

Case 4 was referred to as Configuration 2 in References 11 and 13, and both references provided comparisons of the Pitot pressure data with the predictions of the DSMC technique. At Z = 12 mm, both references showed the comparison between the Case 4 flow angles and the DSMC flow angles. Also, at Z = 12 mm, both references showed and discussed the comparison between the Case 2 and Case 4 Pitot pressures.

4.2.5 Case 5

The next step was to measure the flow angles with a different probe, and a conical probe was chosen. In Case, 5 flow angles were recorded at Z = 0 and 12 mm using conical probe 1. The flow angles recorded were no closer to the DSMC predictions than the Pitot probe 2 values, which was why only two axial stations were surveyed. The cone static pressure (with the probe positioned at the local flow angle) and the flow angle measurements appear in Figures 4-9 and 4-10, respectively. Further comments regarding these results are included in the discussion in Section 4.3.2.

4.2.6 Case 6

In Case 6, Table Set 2 was used, so travel was available over a much larger portion of the plume than before. Conical probe 2 was fabricated to investigate the use of a true conical probe, that is, a probe without a blunt tip. Cone static pressure and flow angle measurements were made at eight axial locations from Z = 12 to 160 mm. Figure 4-11 shows the cone static pressure profiles at Z = 12 and 160 mm, and Figure 4-12 shows the flow angle comparison between the experimental and DSMC values at the same two axial locations. Figure 4-13 shows the experimental and DSMC flow angle comparison over the entire Case 6 experimental region via a contour plot with the experimental results in the bottom half and the DSMC predictions in the top half of the figure. The voids in the lower-left corner of the plot are areas where experimental data was not recorded due to the extremely low static pressures. Any discontinuities in the contour lines in the DSMC half of Figure 4-13 are merely a result of interpolation deficiencies of the plotting program, rather than actual irregularities in the DSMC predictions.

4.2.7 Case 7

In Case 7, Pitot pressure measurements were made with Pitot probe 3. The measurements were made at the same locations that flow angles were recorded in Case 6

using the conical probe/Pitot probe procedure described in Section 3.2.2. Also, since it was known that the flow angle everywhere along the nozzle centerline was zero, a Pitot pressure scan was made over the extent of axial-travel capability of Table Set 2, which was 480 mm. A 133 Pa full-scale capacitance manometer was used to measure the pressures, unlike all of the previous Pitot pressures, which were measured using a 1.33 kPa full-scale capacitance manometer. The lower-range manometer was used because of its smaller measurement uncertainty (one-fourth of the uncertainty of the higher-range manometer).

Figure 4-14 shows the experimental and DSMC (corrected for rarefaction effects) Pitot pressure comparison over the entire Case 6 region in a contour plot with the experimental results in the bottom half and the DSMC predictions in the top half of the figure. The same comments made for Case 6 regarding the voids and the slight DSMC contour discontinuities apply to Figure 4-14 as well. However, the discontinuities at the center of the plot $(\overline{R} = 0)$ are a result of real differences between the experimental and DSMC Pitot pressures on the nozzle centerline. To give more quantitative comparisons, Figure 4-15 shows the experimental and DSMC Pitot pressure profiles at Z = 60 and 160 mm. Figure 4-16 shows the comparison between the experimental and DSMC Pitot pressures for the axial scan along the nozzle centerline. Since the maximum pressure capable of being measured was 133 Pa, some of the Case 4 Pitot pressure data (for Z from 0 to 12 mm) was used to make the comparison complete.

The Case 6 and Case 7 results also appeared in Reference 15, which contained information on the extension of the DSMC code for the larger region of study, details regarding additional considerations in the correction for rarefaction of the numerical results, and also the experimental and DSMC comparisons. The additional considerations mentioned above concerned the applicability ranges of various sized Pitot probes. Actually, Pitot probe 3 was sized solely based on considerations of the correction procedure. That is, if a smaller Pitot probe had been used, the available correction chart, which appeared in Reference 16, could not have been used.

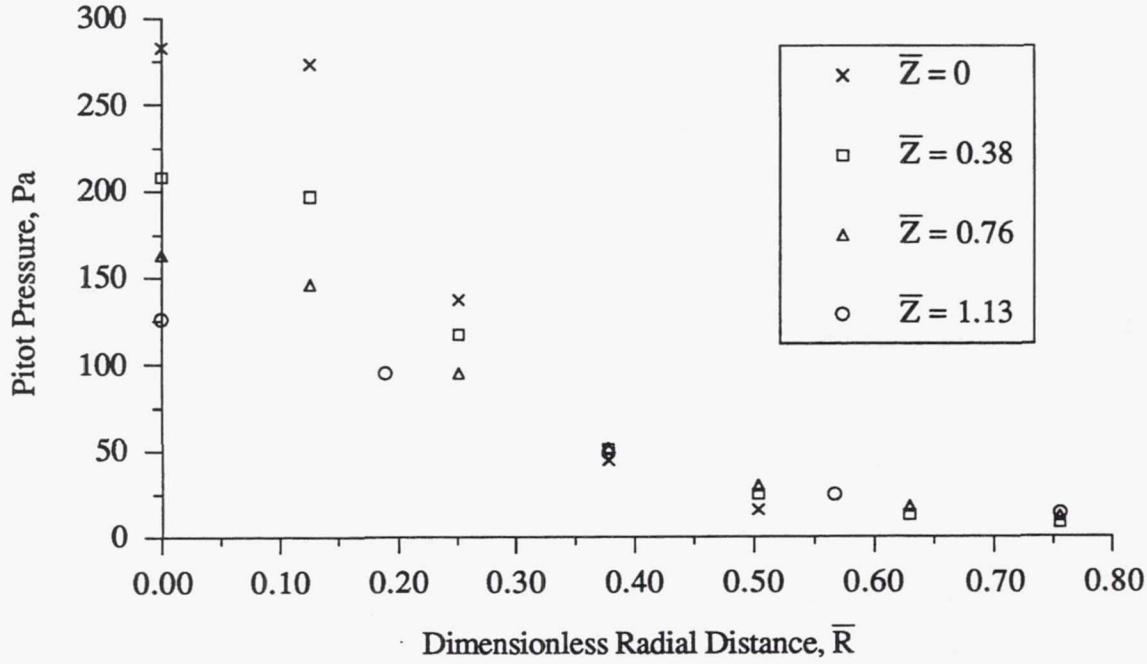

Figure 4-1. Pitot pressure measurements for Case 1.

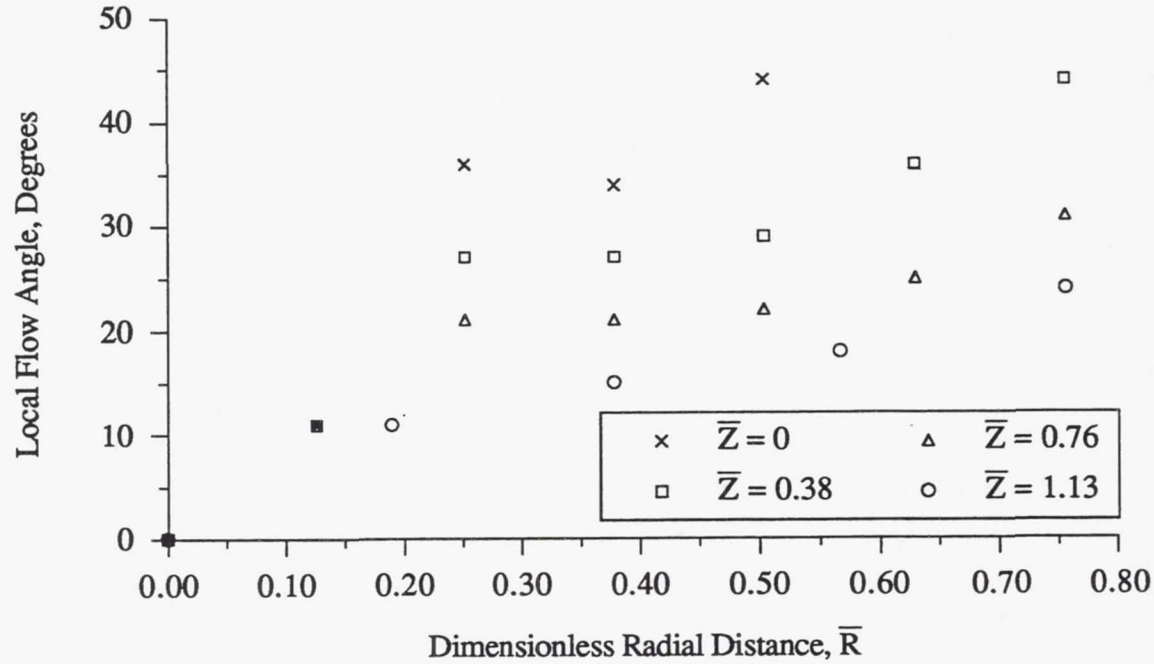

Figure 4-2. Local flow angle measurements for Case 1.

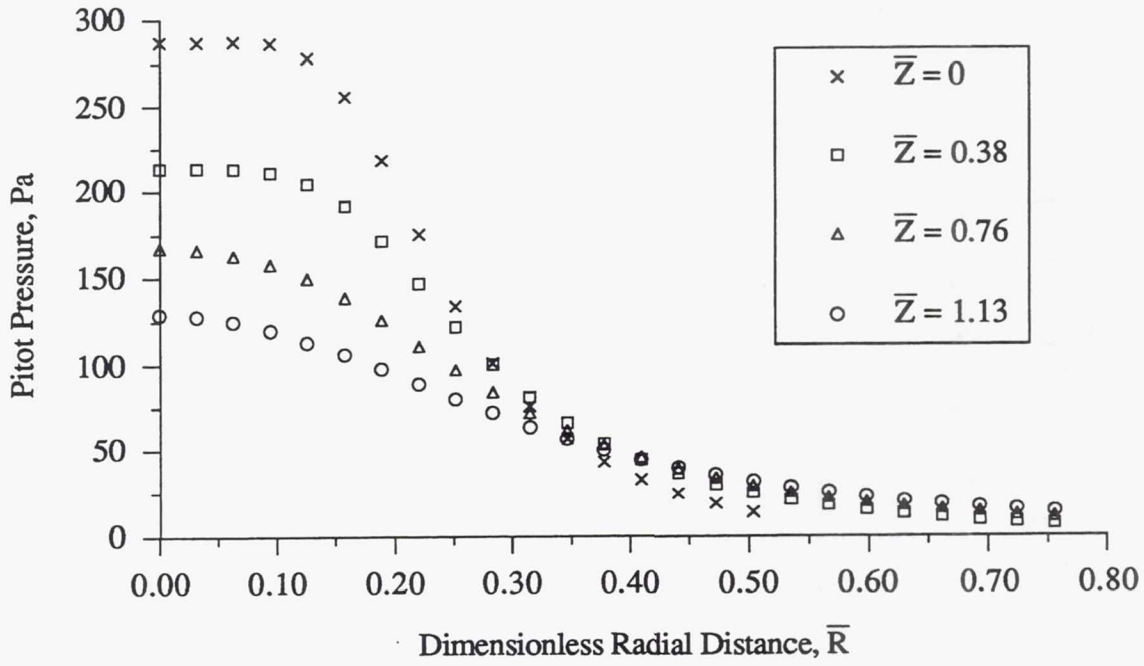

Figure 4-3. Pitot pressure measurements for Case 2.

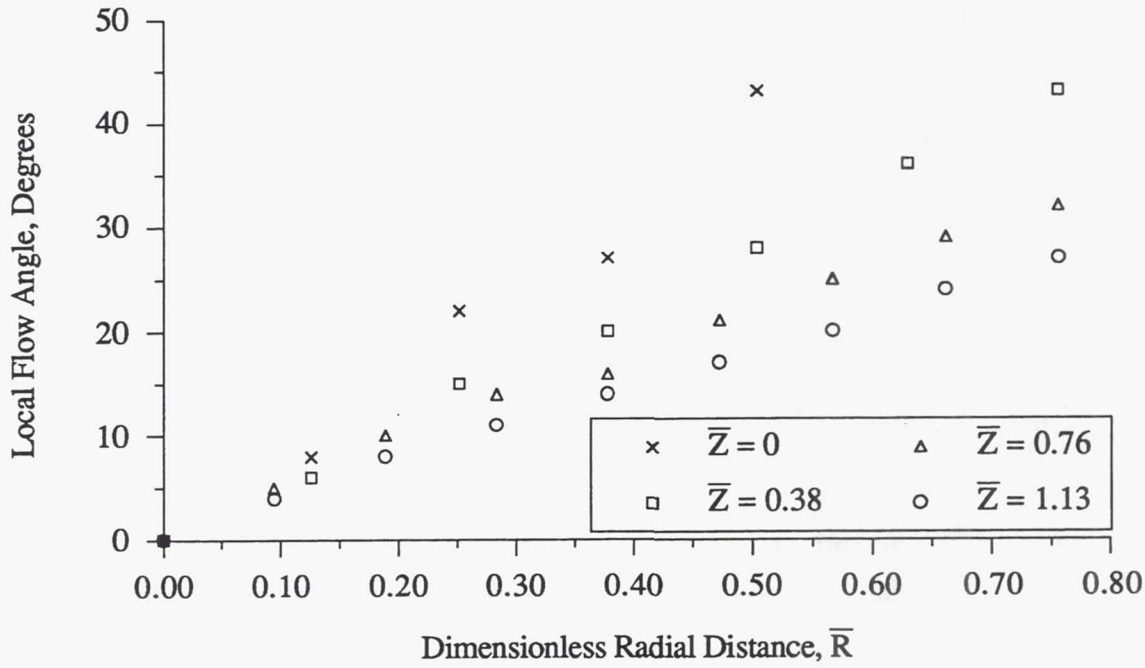

Figure 4-4. Local flow angle measurements for Case 2.

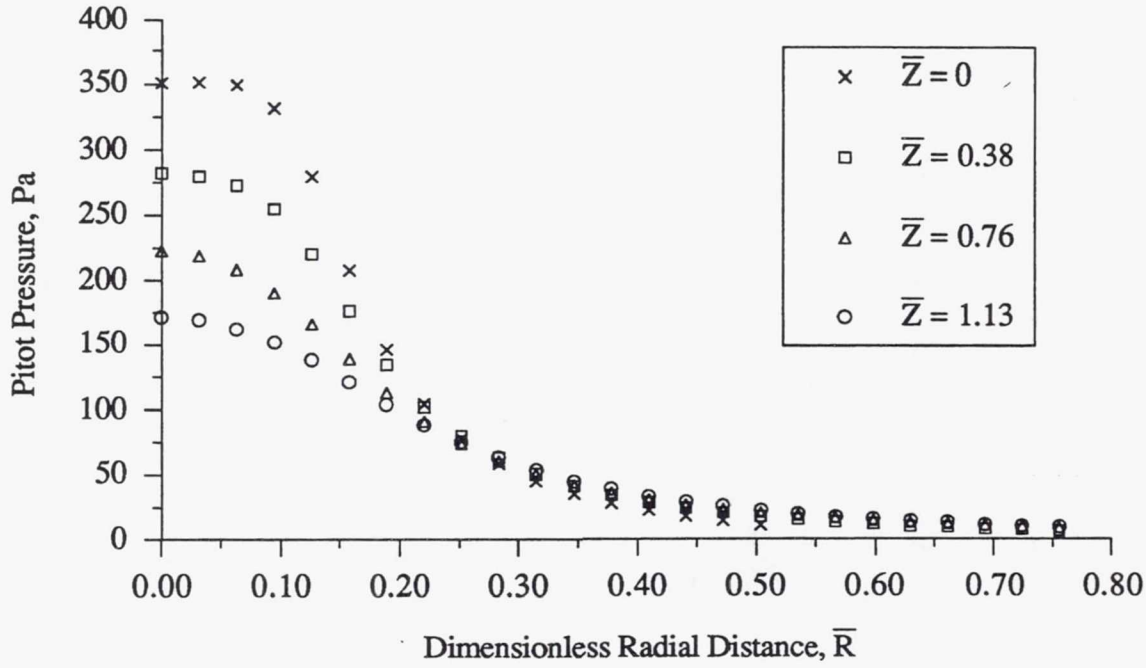

Figure 4-5. Pitot pressure measurements for Case 3.

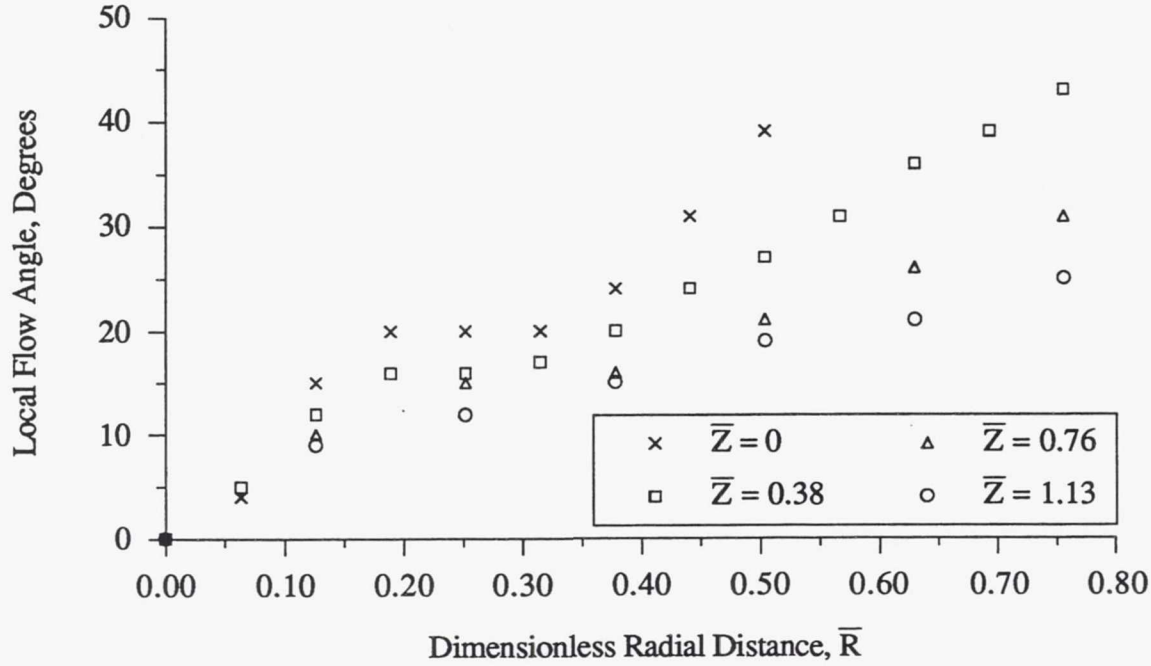

Figure 4-6. Local flow angle measurements for Case 3.

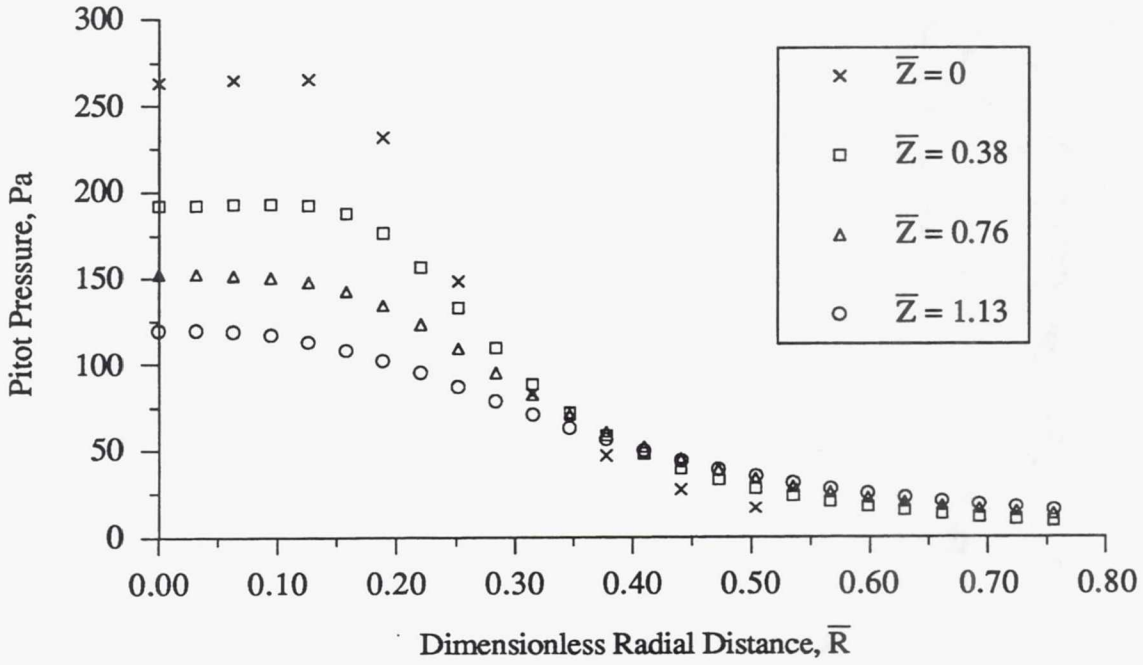

Figure 4-7. Pitot pressure measurements for Case 4.

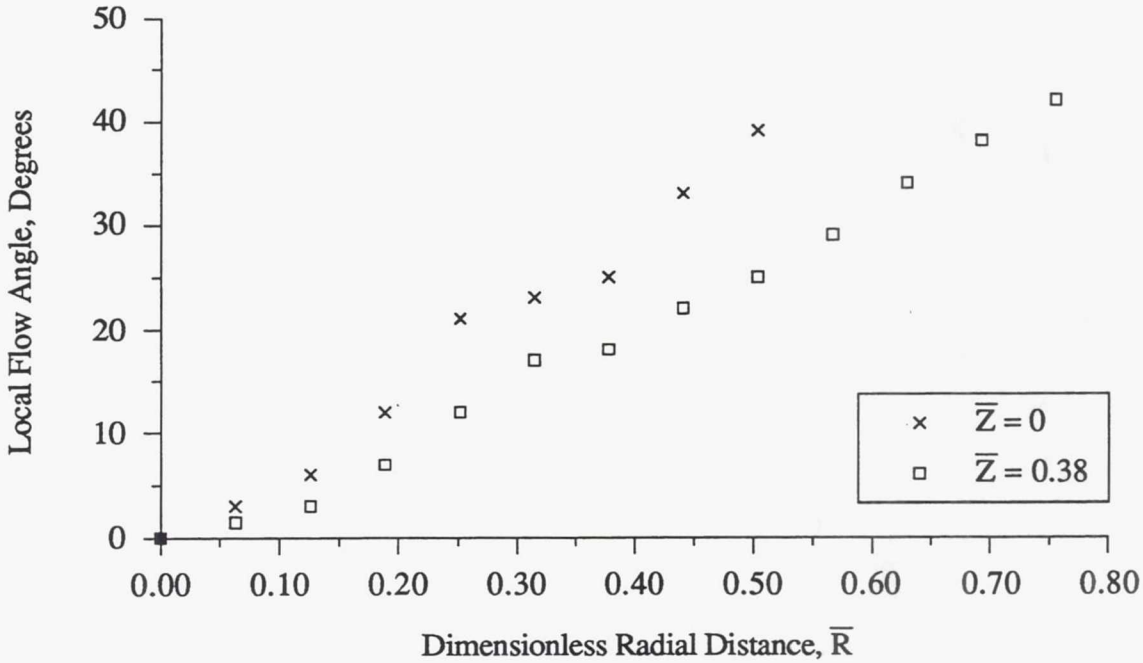

Figure 4-8. Local flow angle measurements for Case 4.

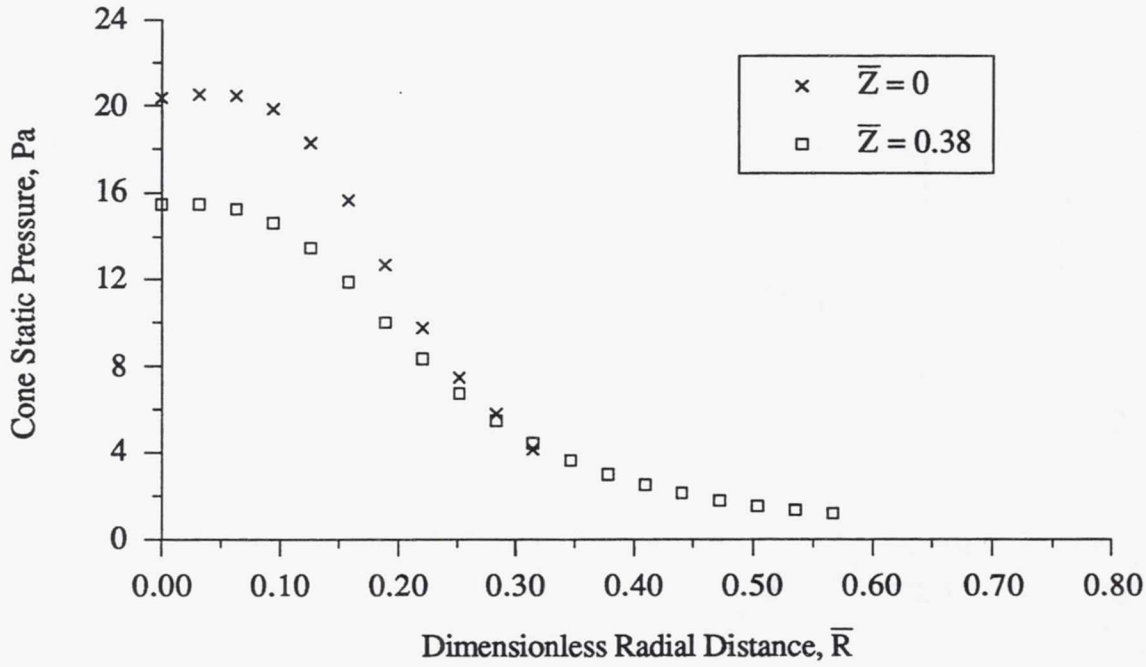

Figure 4-9. Cone static pressure measurements for Case 5.

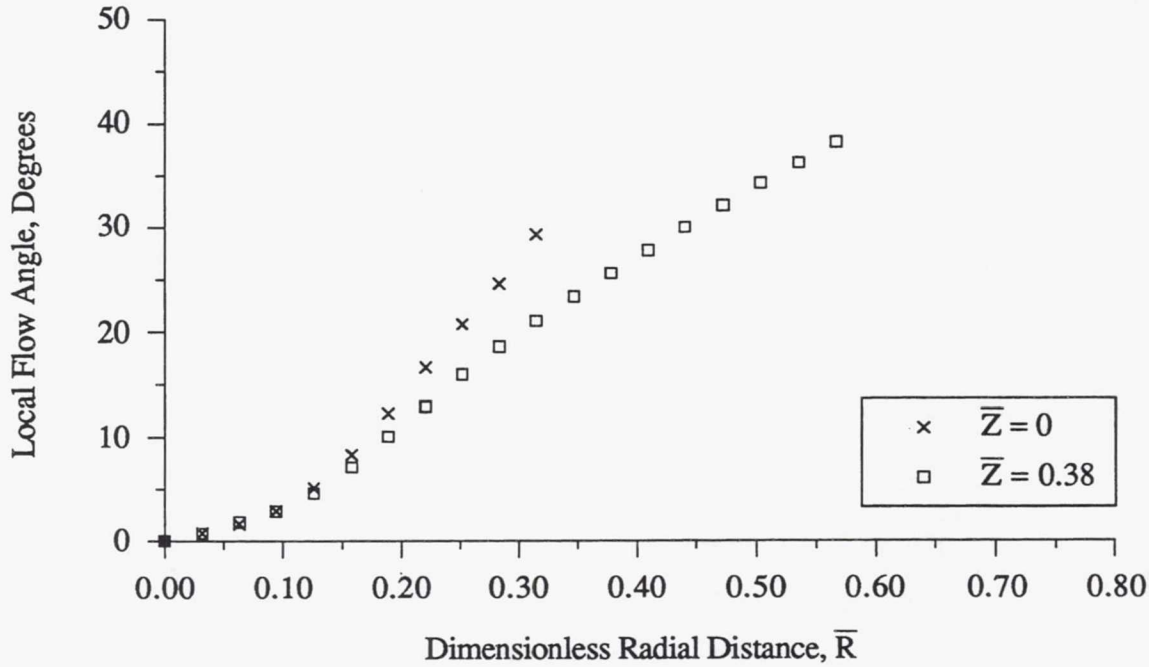

Figure 4-10. Local flow angle measurements for Case 5.

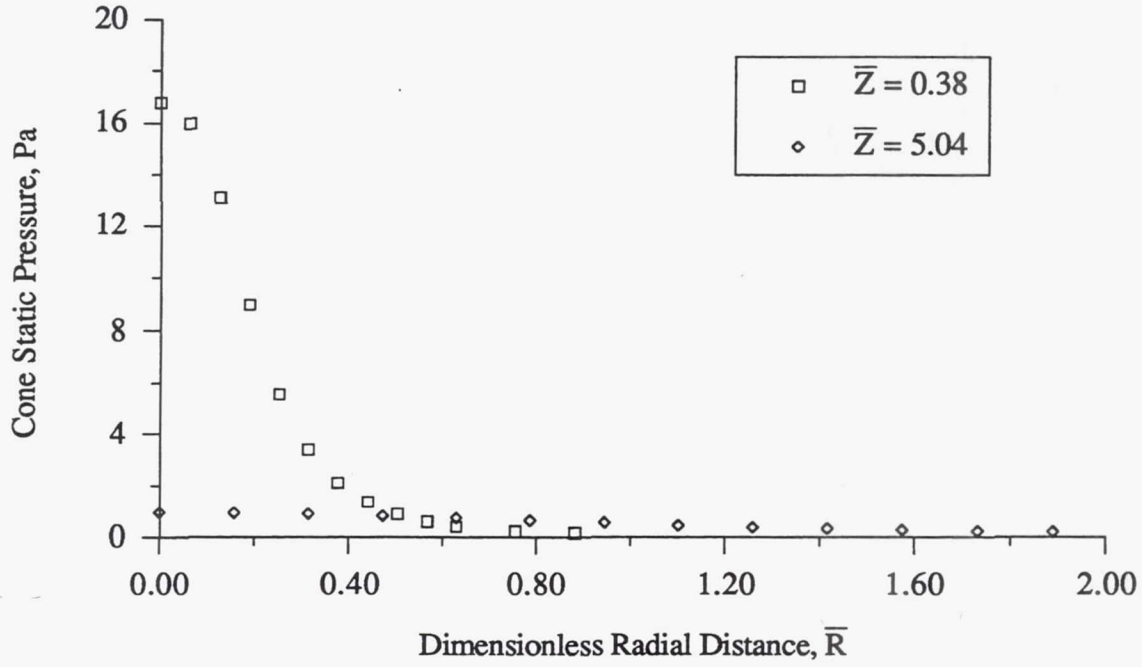

Figure 4-11. Select cone static pressure measurements for Case 6.

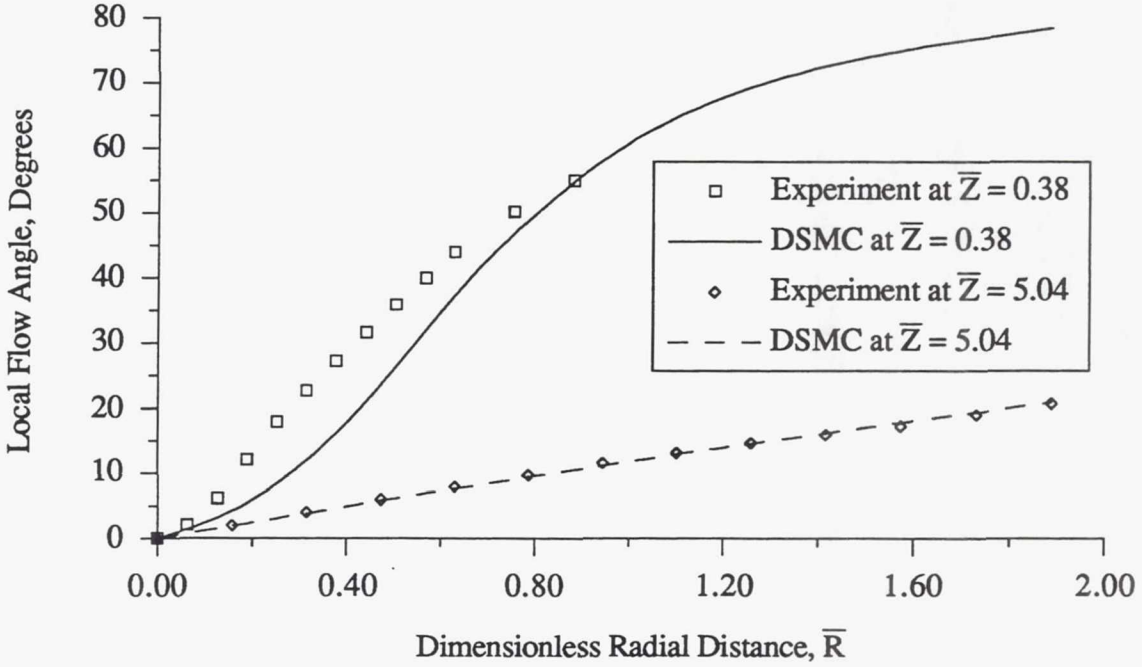

Figure 4-12. Local flow angle comparisons for select axial locations for Case 6.

Page intentionally left blank

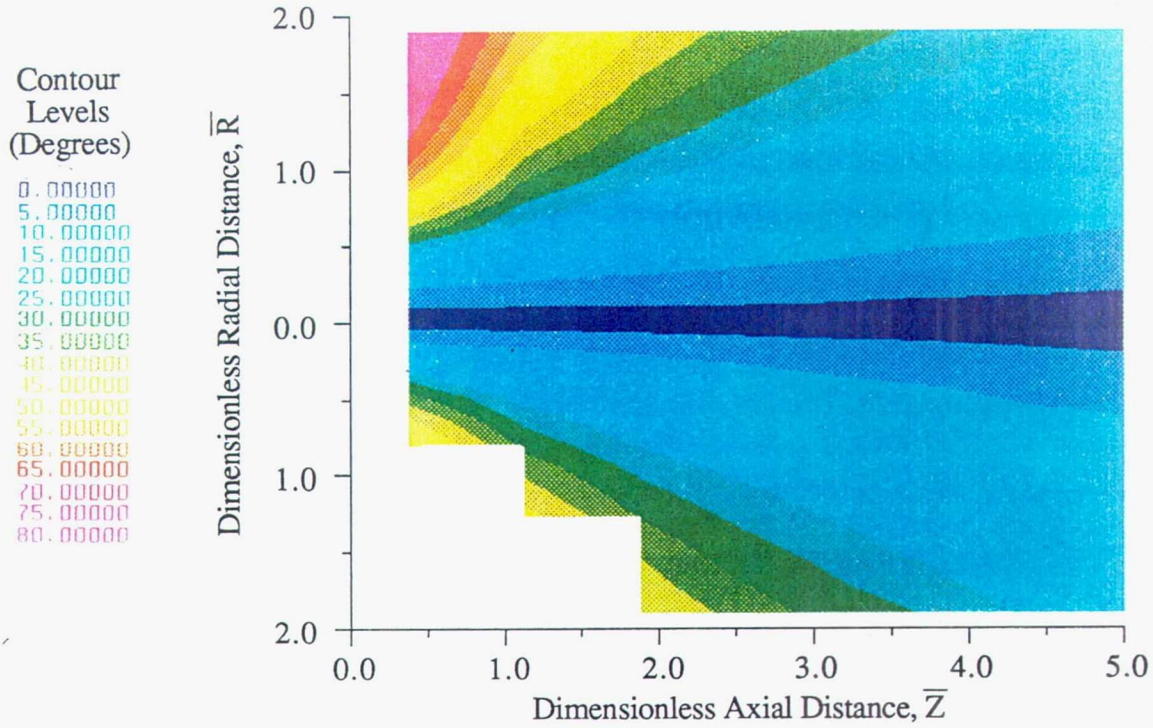

Figure 4-13. Local flow angle comparison for Case 6.

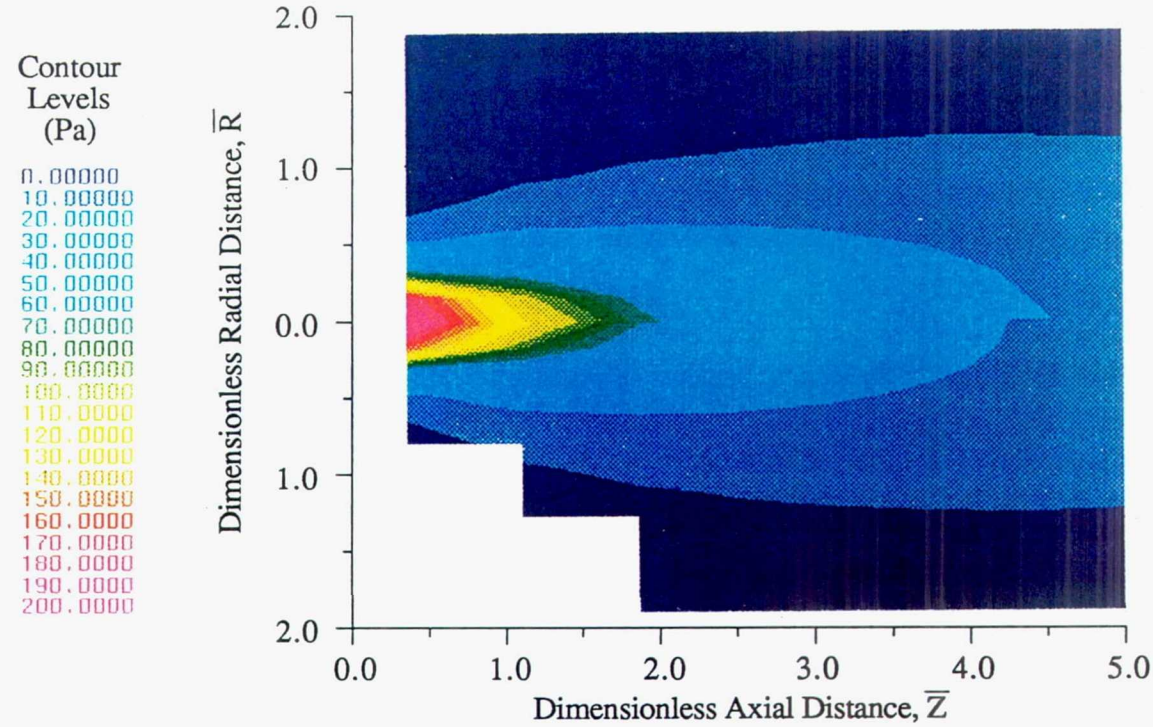

Figure 4-14. Pitot pressure comparison for Case 7.

Page intentionally left blank

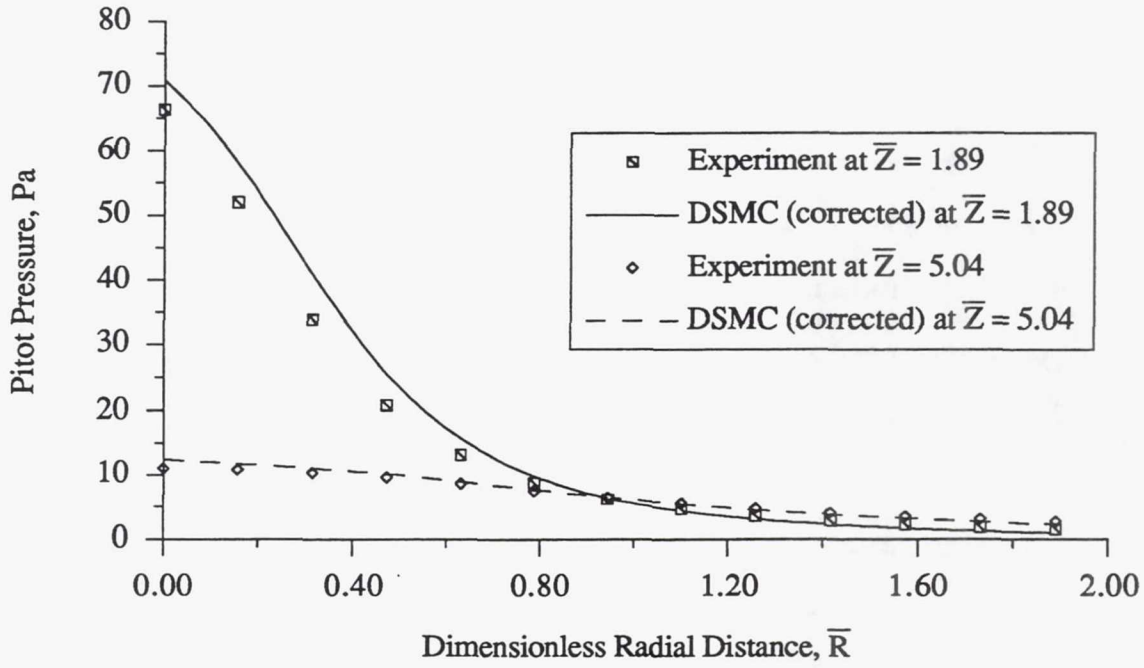

Figure 4-15. Pitot pressure comparisons for select axial locations for Case 7.

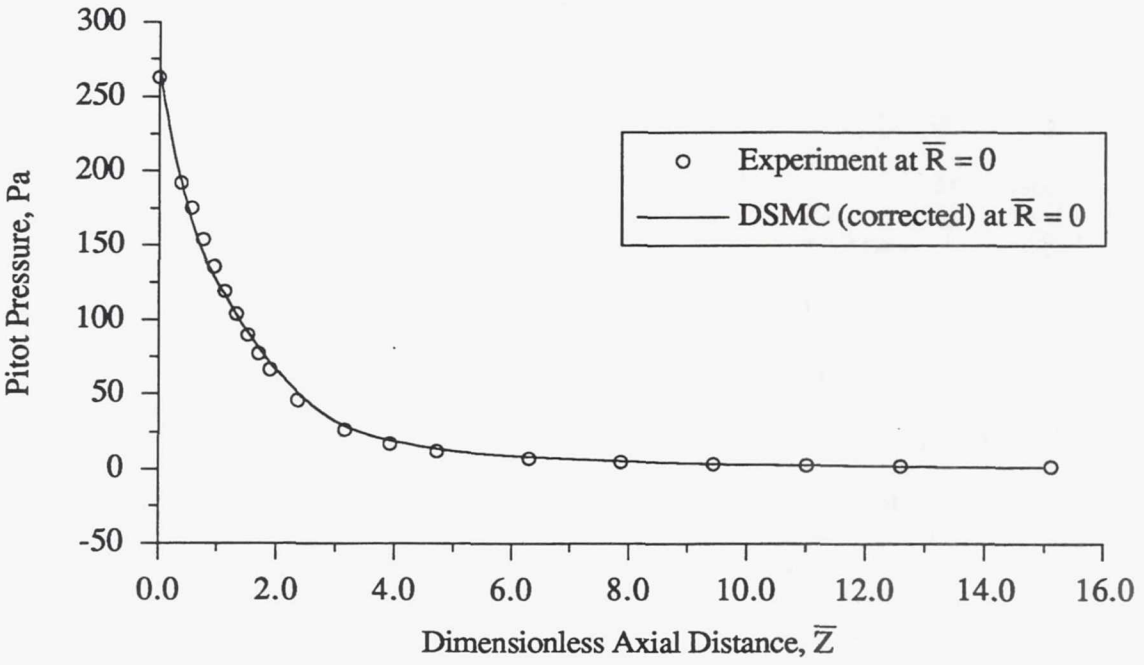

Figure 4-16. Pitot pressure comparison along the nozzle centerline for Cases 4 and 7.

4.3 Discussion

4.3.1 Discussion of the Results

The Pitot pressures measured with Pitot probes 1 and 2 in Cases 1 and 2 agreed with each other to within experimental uncertainty, whereas the larger Pitot probe measured considerably larger flow angles than the smaller probe (most pronounced at the exit plane) over a large portion of each of the radial scans. For example, at $\overline{R} = 0.25, \overline{Z} = 0$ the local flow angle as measured with Pitot probe 1 was 14 degrees larger than that measured with Pitot probe 2, which was not within the experimental uncertainty range at that point. Thus, part of the difference was due to probe-induced effects. For the largest R position for the four radial scans, the largest difference between the flow angles measured with Pitot probes 1 and 2 was 3 degrees, which was within the experimental uncertainty at that point.

In Case 3, with argon (M = 39.95) as the propellant, the Pitot pressures at $\overline{R} = 0$ were higher than those for nitrogen (M = 28.01) by an average of 30 percent, and at the largest R locations the Case 3 pressures were lower by an average of 20 percent. The Case 3 flow angle measurements were nearly identical to the Case 2 flow angles, with the exception of the Case 3 angles being higher for $\overline{R}$ between 0.10 and 0.20 for the axial locations $\overline{Z} = 0$ and 0.38. The largest of these differences was 7 degrees at $\overline{R} = 0.13, \overline{Z} = 0$.

In Case 4 the equipment was the same as for Case 2, except that thruster 2 was used instead of thruster 1. The flow angles for the two Cases were the same to within experimental uncertainty. The difference between the two Cases showed up in the pressure distributions. At $\overline{R} = 0$ the Case 4 pressures were an average of 10 percent lower than those for Case 2, and for the largest R values the Case 4 pressures were an average of 20 percent higher than those for Case 2. The mass flow rates and the stagnation temperatures were nearly identical for the two Cases, but the stagnation pressures differed by about 3 percent. This was probably due to slight machining differences in the two

thrusters, even though they were both designed to the same specifications.

At the exit plane the local flow angles for the flow of nitrogen through thruster 2 were measured in Cases 4 and 5. The angles measured with Pitot probe 2 (in Case 4) were all within 1.4 degrees of those measured with conical probe 1 (in Case 5) for $\overline{R}$ between 0 and 0.25. For higher values of $\overline{R}$, the conical probe flow angles were higher than the Pitot probe flow angles. This comparison is shown in Figure 4-17.

At $\overline{Z} = 0.38$ the flow angles for the flow of nitrogen through thruster 2 were measured in Cases 4, 5 and 6. Figure 4-18 shows the experimental values as well as two other curves. The corresponding flow angles measured by the two conical probes were all within 2 degrees. The differences between the Pitot probe and conical probe flow angles began much earlier (at about $\overline{R} = 0.10$) for $\overline{Z} = 0.38$, as opposed to at the exit plane. Again, for higher values of R the conical probe flow angles were higher than those for the Pitot probe. The biggest difference was at $\overline{R} = 0.57$, where the conical probe 2 flow angle was 11 degrees above the Pitot probe 2 flow angle. This difference was partially caused by the flow field static pressure difference across the finite pressure tap spacing. This consideration was discussed in the uncertainty analysis presented in Section 3.4. The pressure tap spacing for conical probe 1 was 3.1 mm and the spacing for conical probe 2 was 4.3 mm. Thus, any effect due to the spacing distance (such as the flow angle measurements being too high) should have been manifested only 70 percent as much in the conical probe 1 measurements, as compared to the corresponding conical probe 2 values. Over the radial range of $0.10 \leq \overline{R} \leq 0.60$ the conical probe 1 flow angles were below the conical probe 2 values by a consistent amount, with the average difference being 1.7 degrees. An extrapolation of this trend to a zero spacing distance resulted in the data denoted by "No spacing" in Figure 4-18. It can be seen that attempting to account for the static pressure gradient effect in the conical probe flow angle measurements near the nozzle exit plane produced results which matched both the Pitot probe 2 and DSMC results to within the experimental uncertainty. However, for locations near the nozzle exit plane,

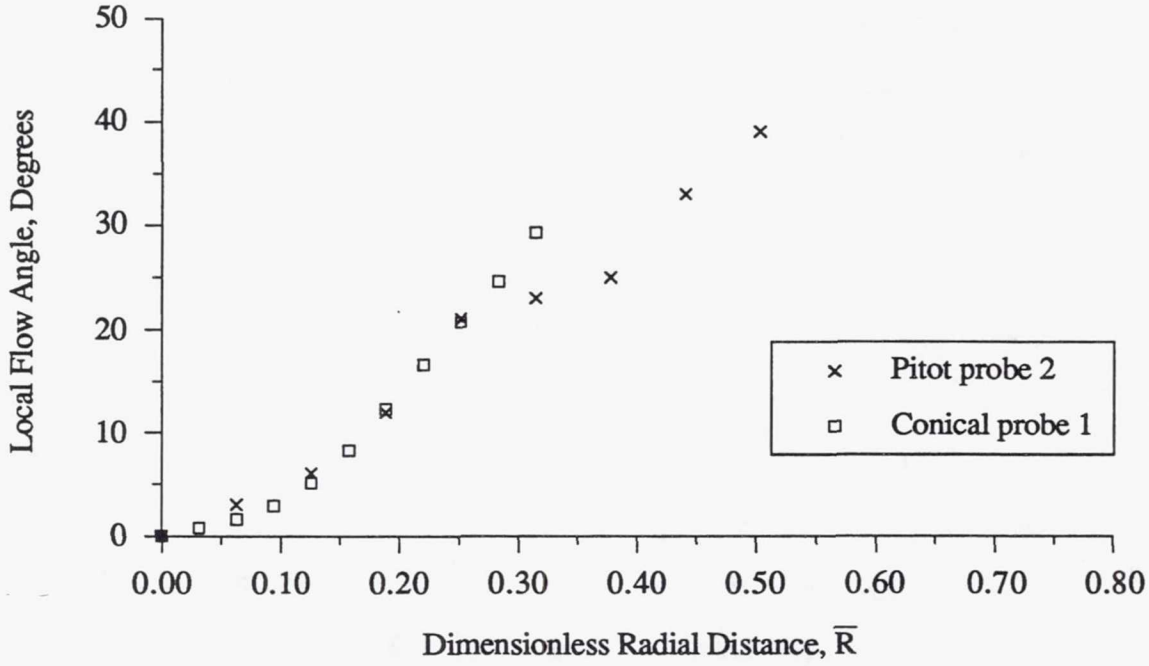

Figure 4-17. Flow angle comparison between Cases 4 and 5 at $\overline{Z} = 0$.

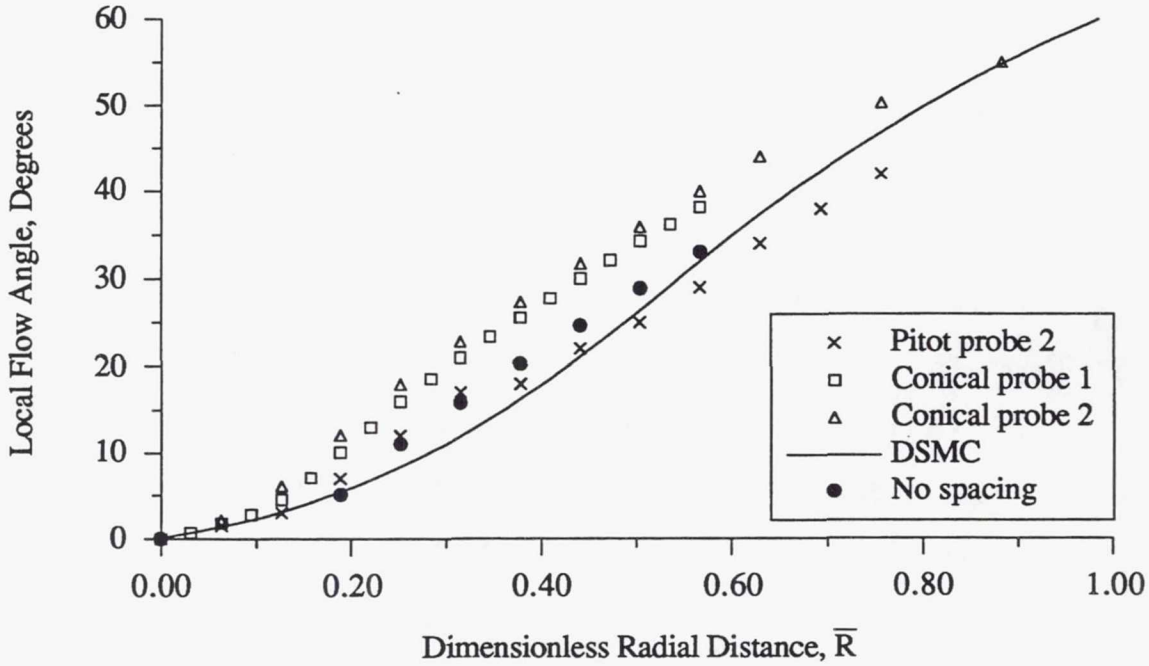

Figure 4-18. Flow angle comparison between DSMC and Cases 4, 5 and 6 at $\overline{Z} = 0.38$.

this procedure for manipulating the conical probe flow angle data was tedious, and thus the conical probe flow angle measuring technique is not recommended for the near-field plume, i.e., the Table Set 1 region. Rather, the use of a small Pitot probe is recommended for those flow angle measurements.

On the other hand, the conical probe worked better in the far-field plume where the gradients of static pressure were very low, as was shown in Figure 4-11. At the axial location $\overline{Z} = 5.04$, the conical probe flow angle uncertainty was ± 0.70 degrees for the entire radial scan. The comparison between the experimental and DSMC flow angles at that location was shown in Figure 4-12. All of the DSMC flow angles were within ± 0.70 degrees of the experimental values. Also, as shown in the uncertainty analysis in Section 3.4, the major contribution to the ± 0.70 degrees uncertainty was the ± 0.50 degrees uncertainty associated with the resolution of the pressure crossover. The identification of the exact pressure crossover angle was truly a random error, and this was displayed nicely by the fact that the data in Figure 4-12 fell both above and below the DSMC curve.

It was shown in References 11, 12 and 13 that the Pitot pressure data for Cases 2 and 4 agreed very well with the results of the DSMC technique, so those comparisons were not repeated here, except for a small region in Figure 4-16 near the exit plane. The portion of Figure 4-16 beyond $\overline{Z} = 0.38$ was all data from Pitot probe 3. The agreement between the measured and predicted pressures was very good. Over the range from $\overline{Z} = 1.89$ to $\overline{Z} = 7.87$ the Pitot pressures computed from the DSMC solution were an average of 10 percent higher than the measured Pitot pressures, and then the DSMC values fell below the measured values for the largest values of Z. Although difficult to see due to the scaling of the ordinate in Figure 4-16, at $\overline{Z} = 15.12$ the DSMC pressure was 14 percent lower than the measured pressure. This was thought to be a consequence of the DSMC code using a perfect vacuum boundary condition at the outer computational boundary.

Figure 4-15 showed the radial comparison between the measured and DSMC Pitot pressures at $\overline{Z} = 1.89$ and $\overline{Z} = 5.04$. The DSMC values fell below the measured values

for large values of R, with the percent differences at $\overline{Z}$ = 1.89 and $\overline{Z}$ = 5.04 being 39 and 19 percent, respectively. This disagreement was also thought to be due to the DSMC perfect vacuum boundary condition.

4.3.2 Discussion of Probe Response Times

The time required for a probe measurement to stabilize, i.e., the probe response time, was dictated mainly by the inside diameter of the tubing between the tap orifice and the transducer, the length of the tubing, and the volume of the manometer. As the inside diameter of the tubing was decreased or the length of the tubing was increased, there was an increasing problem with the probe internal surface roughness inhibiting the molecules from escaping/entering the probe. In addition, the tubing typically had a small cross-sectional area for evacuating the relatively large volume of the manometers. There were two methods used to speed the probe response times. The first was to minimize the tubing length between the tap orifice(s) and the pressure transducer(s), and the second was to use the flow field gradients to advantage during the experiment.

In the hardware configuration used for the current tests, the tubing length was kept to about 0.3 m per line, but shorter tubing lengths were ruled out due to the concern that putting the pressure transducer(s) any closer to the probe tip would disturb the flow field too much. Also, no smaller manometers were available. Thus, the response times for the current tests were fairly high, as previously discussed. However, it would be possible to drastically reduce the tubing length and manometer volume by mounting the pressure transducer(s) inside the probe body. This concept would necessarily require that the manometers be very small, hence reducing the gas volume. For example, Naughton *et al.* [17] have recently designed, fabricated and conducted surveys with a pressure probe with miniature piezoelectric transducers (Endevco Model 8507-50) mounted inside the probe body. Their probe had a distance from the probe tip to the transducer face of about 65 mm. They achieved an increase in response time of two orders of magnitude for wind

tunnel experiments which were previously done with the pressure transducers outside of the wind tunnel. It is felt that the fabrication of similar probes for future tests would result in the capability to perform very extensive Pitot pressure and flow angle surveys in a greatly reduced amount of time.

The second method used to reduce the response time was to use the flow field gradients to advantage during the experiment. When the probe was to be moved to a location of lower/higher pressure, it was first moved to a location of even lower/higher pressure to let the gas be pulled out of/brought into the probe more rapidly. Then the probe was moved back to the desired position and the pressure was allowed to reach equilibrium. The effectiveness of this technique depended on the familiarity of the experimentalist with the flow field being surveyed.

CHAPTER V
Conclusions

Experimental Pitot pressures and flow angles were measured in the expanding plume of a simulated electrothermal propulsion device for the purpose of validating the numerical predictive technology. The research was unique in that the experimental hardware was designed with both experimental and numerical considerations in mind to facilitate direct comparison. Reference was made to the literature containing the comparisons of the experimental and numerical results, and some of the latest comparisons were presented herein. The data were divided into seven Cases, which represented different combinations of the propellant and hardware used.

The nozzle was made as large as possible (while maintaining a throat Reynolds number typical of actual small thrusters) and the measurement probes as small as possible to minimize the probe size relative to the nozzle. However, along with smaller pressure probes came smaller tubing diameters and larger measurement response times. It was found that Pitot probe 2 was sufficient for near-field (regions of large flow field property gradients) Pitot pressure and flow angle measurements, from both response time and measurement accuracy standpoints. In regions of low flow field property gradients, Pitot probe 3 allowed very rapid Pitot pressure measurements, and conical probe 2 worked exceptionally well for the flow angle measurements.

An approach to estimating the experimental uncertainty was presented in this work. The uncertainty analysis was performed for two flow field locations, one where the local property gradients were high and one where they were low. It was found that the Pitot pressure measurement uncertainties at the high and low gradient locations were ± 9 and ± 2

percent of the measurement, respectively. The uncertainty in the conical probe flow angle measurement at the low gradient location was computed to be ± 0.70 degrees, while that in the Pitot probe flow angle measurement at the high gradient location was ± 4.3 degrees. For the conical probe flow angle measurement at the high gradient location (12.3 degrees), the actual flow angle was predicted to lie between 5.0 and 12.6 degrees.

The restriction on taking measurements at further radial locations was the lack of manometers sensitive enough to use the conical probe to measure the flow angles. Manometers with a range of 0 - 13.3 Pa (one-tenth torr) would allow future flow angle and Pitot pressure surveys extending to larger radial distances. The initial driver for the current research effort was the desire to eventually gain knowledge of the flow phenomena in the backflux region, and that may also be possible using the current conical probe/Pitot probe technique with one-tenth torr manometers.

If extensive pressure probe data is desired in the future, it is recommended to consider the fabrication of probes with internally-mounted pressure transducers, such as the probe designed by Naughton *et al.* [17]. Such probes would essentially eliminate the response time problem. On the other hand, it would be more desirable to obtain non-intrusive data in the near future. Techniques such as laser-induced fluorescence (LIF) and electron beam fluorescence would produce velocity data which could be compared directly with the numerical results. No bothersome corrections for probe effects on the local flow field would be required.

Also, in the future it is recommended to implement a laser-alignment technique, whereby the probe position with respect to the nozzle could be more accurately determined. The alignment would only be needed for the initial probe positioning, as the incremental positioning of the probe was a very accurate procedure. As was shown in the uncertainty analysis herein, reducing the probe position inexactness would greatly reduce the uncertainty in many of the measurements, particularly the Pitot pressure measurements.

REFERENCES

[1] Lengrand, J., "Plume Impingement Upon Spacecraft Surfaces", in *Rarefied Gas Dynamics*, edited by H. Oguchi, University of Tokyo Press, Tokyo, Japan, pp. 217-228, 1985.

[2] Yoshida, R., Halbach, C. and Hill, S., "Life Test Summary and High Vacuum Tests of 10mlb Resistojets", *Journal of Spacecraft and Rockets*, Vol. 8, pp. 414-416, April 1971.

[3] Manzella, D., "An Experimental Investigation of the Effect of Cell Pressure on the Performance of Resistojets", M.Sc. Thesis, University of Toledo, Toledo, Ohio, 1988.

[4] Bailey, A., Price, L., Pipes, J., McGregor, W. and Matz, R., "Flow Field Mapping of Gas/Particle Nozzle Expansions into Vacuum", AEDC-TR-84-38, July 1985.

[5] Bailey, A. and Price, L., "Flow Field Mapping of Carbon Dioxide into Vacuum", AEDC-TR-85-26, July 1985.

[6] Bailey, A., "Flow-Angle Measurements in a Rarefied Nozzle Plume", *AIAA Journal*, Vol. 25, pp. 1301-1304, December 1987.

[7] Legge, H. and Dettleff, G., "Pitot Pressure and Heat Transfer Measurements in Hydrazine Thruster Plumes", *Journal of Spacecraft and Rockets*, Vol. 23, pp. 357-362, July-August 1986.

[8] Boyd, I., Penko, P. and Carney, L., "Efficient Monte Carlo Simulation of Rarefied Flow in a Small Nozzle", AIAA Paper 90-1693, AIAA/ASME 5th Joint Thermophysics and Heat Transfer Conference, Seattle, WA, June 1990.

[9] Cline, M., "VNAP: A Program for Computation of Two-Dimensional, Time-Dependent Compressible, Viscous Internal Flow", Los Alamos Laboratory Report LA-7326, Nov. 1978.

[10] Bird, G., *Molecular Gas Dynamics*, Clarendon Press, Oxford, 1976.

[11] Boyd, I., Penko, P., Meissner, D. and DeWitt, K., "Experimental and Numerical Investigations of Low-Density Nozzle and Plume Flows of Nitrogen", *AIAA Journal*, (in press).

[12] Boyd, I., Penko, P. and Meissner, D., "Numerical and Experimental Investigations of Nozzle and Plume Flows of Nitrogen", AIAA Paper 91-1363, AIAA 26th Thermophysics Conference, Honolulu, HI, June 1991.

[13] Penko, P., Boyd, I., Meissner, D. and DeWitt, K., "Pressure Measurements in a Low-Density Nozzle Plume for Code Verification", AIAA Paper 91-2110, AIAA/SAE/ASME/ASEE 27th Joint Propulsion Conference, Sacramento, CA, June 1991.

[14] Finke, R., Holmes, A. and Keller, T., "Space Environment Facility for Electric Propulsion Systems Research", NASA TN-D-2774, 1965.

[15] Penko, P., Boyd, I., Meissner, D. and DeWitt, K., "Measurement and Analysis of a Small Nozzle Plume in Vacuum", AIAA Paper 92-3108, AIAA/SAE/ASME/ASEE 28th Joint Propulsion Conference, Nashville, TN, July 1992.

[16] Stephenson, W., "Use of the Pitot Tube in Very Low Density Flows", AEDC-TR-81-11, October 1981.

[17] Naughton, J., Cattafesta III, L. and Settles, G., "A Miniature, Fast-Response 5-Hole Probe for Supersonic Flowfield Measurements", AIAA Paper 92-0266, 30th Aerospace Sciences Meeting, Reno, NV, January 1992.

APPENDIX A
Plume Studies Data Summary (7/25/90 to 5/5/92)

Here is how the Run #s from the raw data sheets fall into the Cases defined herein:

Runs 1-6: Not included since the stagnation temperatures were 791 K (Runs 1,2,3) and 921 K (Runs 4,5,6), and ultimately the rest of all nitrogen tests were run at 700 K. Also, no probe rotation was performed for these runs.

Runs 7-10: Case 1.

Runs 11-14: Case 2.

Runs 15-18: Case 3.

Runs 19-21: Not included. The smallest Pitot probe (.032 in. OD) was used, and peculiar results and large response times were observed.

Runs 22-26: Case 4.

Run 27: Not included since Run 28 was identical, except that in Run 28 more measurements were made.

Runs 28&29: Case 5.

Run 30: Not included. In this run the two static-tap lines were connected to a single manometer. The response times were large and much more reliable flow angle data was later obtained using two manometers.

Runs 31&32: Not included. In these two runs the conical probe was used like a Pitot probe (to measure stagnation pressures). However, the data was ultimately of no use since comparable computational results were not available. Incidentally, Run 32 was a rerun of Run 31 without the magnetic effect of the motors.

Run 33: Not included. It was decided that the manometer zero-shifts during the run were too large to ignore. Thus, all Case 6 runs were done using periodic re-zeroing of the manometers throughout the run.

Runs 34-36: Case 6.

Runs 37-39: Not included for the same reason as Runs 31&32.

Run 40: Case 7.

* Table Set 1 was used for Runs 1-30, Table Set 2 for Runs 31-40.
* Thruster 1 was used for Runs 1-21, Thruster 2 for Runs 22-40.
* The stagnation pressure manometer was the Wallace & Tiernan up to and including the 12/7/90 runs, and after that the 100-torr capacitance manometer was used.
* Pitot probe flow angle data are given to the nearest degree, and conical probe flow angle data are given to the nearest 0.1 degree.
* Pressure data are given using the following convention:

Stagnation Pressure		Probe Pressure	
Wallace & Tiernan:	nearest 100 Pa	10-torr capacitance:	nearest 0.1 Pa
100-torr capacitance:	nearest 1 Pa	1-torr capacitance:	nearest 0.01 Pa

RUNS 1,2,3 - 7/25/90

Propellant: nitrogen
Power: 109 W
Mass Flow Rate: 5.5E-5 kg/s
Stagnation Pressure: 5600 Pa
Stagnation Temp.: 791 K
Probe: Pitot probe 1
Axial Position: 0 mm (Run1)
Rotary Position: 0 degrees

Radial Position (mm)	Pitot Pressure (Pa)
20	0.7
18	0.7
16	8.7
14	18.9
12	35.1
10	62.1
8	108.3
6	178.9
4	248.1
2	273.7
0	276.6
-2	273.4
-4	245.6
-6	175.3
-8	105.7
-10	60.7
-12	34.3
-14	19.2
-16	9.1
-18	0.7
-20	0.7

Axial Position: 12 mm (Run 2)
Rotary Position: 0 degrees

Radial Position (mm)	Pitot Pressure (Pa)
24	2.9
20	6.9
16	17.7
12	43.3
8	98.0
4	178.4
0	202.5
-4	173.1
-8	92.7
-12	40.7
-16	17.2
-20	6.7
-24	2.8

Radial Position: 0 mm (Run 3)
Rotary Position: 0 degrees

Axial Position (mm)	Pitot Pressure (Pa)
0	276.6
2	261.6
4	247.7
6	235.0
8	223.4
10	212.6
12	202.5
14	192.8
16	183.7
18	174.8
20	166.1
22	157.5
24	149.2
26	141.3
28	133.6
30	126.1
36	106.0

RUNS 4,5,6 - 8/10/90

Propellant: nitrogen
Power: 166 W
Mass Flow Rate: 6.8E-5 kg/s
Stagnation Pressure: 7100 Pa
Stagnation Temp.: 921 K
Probe: Pitot probe 1
Axial Position: 0 mm (Run 4)
Rotary Position: 0 degrees

Radial Position (mm)	Pitot Pressure (Pa)
20	0.8
18	0.8
16	12.7
14	25.3
12	46.7
10	85.1
8	151.5
6	248.2
4	327.3
2	350.0
0	351.2
-2	349.7
-4	324.2
-6	239.8
-8	143.6
-10	79.9
-12	43.5
-14	23.2
-16	11.3
-18	0.7
-20	0.7

Axial Position: 12 mm (Run 5)
Rotary Position: 0 degrees

Radial Position (mm)	Pitot Pressure (Pa)
24	3.5
21	6.7
18	14.0
15	29.1
12	57.5
9	110.0
6	189.9
3	248.5
0	258.9
-3	246.4
-6	183.2
-9	104.0
-12	54.4
-15	26.7
-18	12.9
-21	6.1
-24	3.1

Axial Position: 24 mm (Run 6)
Rotary Position: 0 degrees

Radial Position (mm)	Pitot Pressure (Pa)
24	7.7
21	12.5
18	21.1
15	35.5
12	58.4
9	94.5
6	142.4
3	183.5
0	196.8
-3	180.5
-6	136.8
-9	88.9
-12	54.7
-15	32.4
-18	19.1
-21	11.2
-24	6.8

RUN 7 - 8/30/90

Propellant: nitrogen
Power: 75.1 W
Mass Flow Rate: 6.8E-5 kg/s
Stagnation Pressure: 6100 Pa
Stagnation Temp.: 696 K
Probe: Pitot probe 1
Axial Position: 0 mm

Radial Position (mm)	Max. Pitot Pressure (Pa)	Local Flow Angle (degrees)
0	281.8	0
4	272.6	11
8	136.9	36
12	44.7	34
16	15.8	44

RUNS 8,9,10 - 8/31/90

Propellant: nitrogen
Power: 75.4 W
Mass Flow Rate: 6.8E-5 kg/s
Stagnation Pressure: 6100 Pa
Stagnation Temp.: 699 K
Probe: Pitot probe 1
Axial Position: 12 mm (Run 8)

Radial Position (mm)	Max. Pitot Pressure (Pa)	Local Flow Angle (degrees)
0	208.1	0
4	196.7	11
8	116.5	27
12	51.3	27
16	25.3	29
20	13.3	36
24	7.7	44

Axial Position: 24 mm (Run 9)

Radial Position (mm)	Max. Pitot Pressure (Pa)	Local Flow Angle (degrees)
0	163.3	0
4	146.0	11
8	94.9	21
12	51.7	21
16	29.9	22
20	18.1	25
24	12.0	31

Axial Position: 36 mm (Run 10)

Radial Position (mm)	Max. Pitot Pressure (Pa)	Local Flow Angle (degrees)
0	125.7	0
6	94.4	11
12	48.7	15
18	25.1	18
24	14.0	24

RUNS 11,12 - 9/6/90

Propellant: nitrogen
Power: 75.8 W
Mass Flow Rate: 6.8E-5 kg/s
Stagnation Pressure: 6400 Pa
Stagnation Temp.: 699 K
Probe: Pitot probe 2
Axial Position: 0 mm (Run 11)

Radial Position (mm)	Max. Pitot Pressure (Pa)	Local Flow Angle (degrees)
0	286.4	0
4	276.6	8
8	135.1	22
12	45.3	27
16	15.9	43

Axial Position: 12 mm (Run 12)

Radial Position (mm)	Max. Pitot Pressure (Pa)	Local Flow Angle (degrees)
0	215.0	0
4	204.1	6
8	123.2	15
12	56.1	20
16	26.8	28
20	14.3	36
24	7.7	43

RUNS 13,14 - 11/16/90

Propellant: nitrogen
Power: 76.0 W
Mass Flow Rate: 6.8E-5 kg/s
Stagnation Pressure: 6300 Pa
Stagnation Temp.: 695 K
Probe: Pitot probe 2
Axial Position: 24 mm (Run 13)

Radial Position (mm)	Max. Pitot Pressure (Pa)	Local Flow Angle (degrees)
0	168.7	0
3	158.9	5
6	127.1	10
9	84.4	14
12	53.7	16
15	34.1	21
18	22.9	25
21	15.7	29
24	11.9	32

Axial Position: 36 mm (Run 14)

Radial Position (mm)	Max. Pitot Pressure (Pa)	Local Flow Angle (degrees)
0	130.0	0
3	120.7	4
6	98.7	8
9	72.5	11
12	51.9	14
15	36.5	17
18	26.5	20
21	19.6	24
24	15.2	27

RUNS 11a,12a - 10/18/90

Propellant: nitrogen
Power: 75.4 W
Mass Flow Rate: 6.8E-5 kg/s
Stagnation Pressure: 6400 Pa
Stagnation Temp.: 697 K
Probe: Pitot probe 2
Axial Position: 0 mm (Run 11a)

Radial Position (mm)	Maximum Pitot Pressure (Pa)
0	287.0
1	287.2
2	287.4
3	286.2
4	278.0
5	255.4
6	218.1
7	174.8
8	134.0
9	100.8
10	75.5
11	56.8
12	43.3
13	32.9
14	24.7
15	18.8
16	13.3

Axial Position: 12 mm (Run 12a)

Radial Position (mm)	Maximum Pitot Pressure (Pa)
0	213.4
1	213.4
2	213.2
3	210.9
4	204.4
5	191.3
6	171.1
7	146.5
8	122.1
9	99.9
10	81.1
11	66.1
12	54.0
13	44.1
14	36.7
15	30.3
16	25.2
17	20.9
18	17.6
19	14.9
20	12.7
21	10.8
22	9.2
23	7.7
24	6.8

RUNS 13a,14a - 11/2/90

Propellant: nitrogen
Power: 75.4 W
Mass Flow Rate: 6.8E-5 kg/s
Stagnation Pressure: 6300 Pa
Stagnation Temp.: 695 K
Probe: Pitot probe 2
Axial Position: 24 mm (Run 13a)

Radial Position (mm)	Maximum Pitot Pressure (Pa)
0	167.2
1	166.1
2	162.7
3	157.7
4	149.7
5	138.7
6	125.9
7	111.3
8	97.3
9	84.1
10	71.9
11	61.9
12	53.1
13	45.7
14	39.3
15	34.0
16	29.3
17	25.6
18	22.4
19	19.7
20	17.5
21	15.5
22	13.9
23	12.4
24	11.3

Axial Position: 36 mm (Run 14a)

Radial Position (mm)	Maximum Pitot Pressure (Pa)
0	129.1
1	127.7
2	124.5
3	119.7
4	113.3
5	105.9
6	97.7
7	88.9
8	80.1
9	71.9
10	63.7
11	56.7
12	50.1
13	44.4
14	39.9
15	35.5
16	31.7
17	28.4
18	25.5
19	22.9
20	20.4
21	18.7
22	16.8
23	15.3
24	13.9

RUNS 15,16 - 12/28/90

Propellant: argon
Power: 67.7 W
Mass Flow Rate: 6.8E-5 kg/s
Stagnation Pressure: 4770 Pa
Stagnation Temp.: 648 K
Probe: Pitot probe 2
Axial Position: 0 mm (Run 15)

Radial Position (mm)	Max. Pitot Pressure (Pa)	Local Flow Angle (degrees)
0	354.8	0
2	351.8	4
4	288.2	15
6	153.9	20
8	81.1	20
10	47.3	20
12	30.1	24
14	19.3	31
16	12.5	39

Axial Position: 12 mm (Run 16)

Radial Position (mm)	Max. Pitot Pressure (Pa)	Local Flow Angle (degrees)
0	-------	0
2	274.0	5
4	221.7	12
6	134.1	16
8	80.1	16
10	50.9	17
12	34.5	20
14	25.1	24
16	18.4	27
18	14.0	31
20	10.9	36
22	8.8	39
24	7.2	43

RUNS 17,18 - 12/21/90

Propellant: argon
Power: 67.7 W
Mass Flow Rate: 6.8E-5 kg/s
Stagnation Pressure: 4746 Pa
Stagnation Temp.: 648 K
Probe: Pitot probe 2
Axial Position: 24 mm (Run 17)

Radial Position (mm)	Max. Pitot Pressure (Pa)	Local Flow Angle (degrees)
0	224.6	0
4	175.6	10
8	78.0	15
12	37.2	16
16	20.5	21
20	12.4	26
24	8.0	31

Axial Position: 36 mm (Run 18)

Radial Position (mm)	Max. Pitot Pressure (Pa)	Local Flow Angle (degrees)
0	171.3	0
4	138.4	9
8	74.7	12
12	38.9	15
16	22.3	19
20	14.0	21
24	9.5	25

RUNS 15a,16a,17a - 12/7/90

Propellant: argon
Power: 67.4 W
Mass Flow Rate: 6.8E-5 kg/s
Stagnation Pressure: 4500 Pa
Stagnation Temp.: 647 K
Probe: Pitot probe 2
Axial Position: 0 mm (Run 15a)

Radial Position (mm)	Maximum Pitot Pressure (Pa)
0	351.4
1	351.6
2	349.6
3	331.7
4	280.0
5	207.7
6	146.4
7	104.1
8	77.5
9	58.4
10	45.1
11	35.5
12	28.4
13	22.5
14	18.1
15	14.5
16	11.5

Axial Position: 12 mm (Run 16a)

Radial Position (mm)	Maximum Pitot Pressure (Pa)
0	282.2
1	280.0
2	273.3
3	255.0
4	220.6
5	176.7
6	135.1
7	102.4
8	79.6
9	63.1
10	50.7
11	41.3
12	34.4
13	28.5
14	24.1
15	20.7
16	17.6
17	15.5
18	13.3
19	11.6
20	10.3
21	9.1
22	8.0
23	7.1
24	6.1

Axial Position: 24 mm (Run 17a)

Radial Position (mm)	Maximum Pitot Pressure (Pa)
0	222.9
1	219.0
2	208.1
3	190.5
4	166.3
5	139.5
6	113.1
7	90.9
8	73.7
9	60.4
10	49.9
11	41.9
12	36.0
13	30.9
14	26.8
15	23.3
16	20.7
17	18.3
18	16.4
19	14.5
20	13.1
21	11.9
22	10.7
23	9.7
24	8.8

RUN 18a - 12/21/90

Propellant: argon
Power: 67.7 W
Mass Flow Rate: 6.8E-5 kg/s
Stagnation Pressure: 4746 Pa
Stagnation Temp.: 648 K
Probe: Pitot probe 2
Axial Position: 36 mm

Radial Position (mm)	Maximum Pitot Pressure (Pa)
0	171.5
1	169.7
2	162.8
3	152.3
4	138.4
5	120.8
6	103.7
7	87.9
8	74.8
9	62.9
10	53.1
11	44.8
12	39.1
13	32.9
14	28.9
15	25.7
16	22.3
17	19.5
18	17.3
19	15.6
20	14.0
21	12.7
22	11.5
23	10.4
24	9.5

RUNS 19,20,21 - 1/4/91

Propellant: argon
Power: 67.7 W
Mass Flow Rate: 6.8E-5 kg/s
Stagnation Pressure: 4770 Pa
Stagnation Temp.: 649 K
Probe: 0.032" OD Pitot with 0.003" wall
Axial Position: 0 mm (Run 19)

Radial Position (mm)	Max. Pitot Pressure (Pa)	Local Flow Angle (degrees)
0	356.0	0
2	352.6	5
4	291.0	26
6	161.1	36
8	81.7	30

Axial Position: 12 mm (Run 20)

Radial Position (mm)	Max. Pitot Pressure (Pa)	Local Flow Angle (degrees)
2	274.6	7
4	218.6	24

Axial Position: 24 mm (Run 21)

Radial Position (mm)	Max. Pitot Pressure (Pa)	Local Flow Angle (degrees)
2	212.1	11
4	169.5	18

RUN 22 - 4/25/91

Propellant: nitrogen
Power: 63.5 W
Mass Flow Rate: 6.8E-5 kg/s
Stagnation Pressure: 6198 Pa
Stagnation Temp.: 700 K
Probe: Pitot probe 2
Axial Position: 0 mm

Radial Position (mm)	Max. Pitot Pressure (Pa)	Local Flow Angle (degrees)
-4	265.6	-6
-2	265.0	-2
0	262.9	0
2	264.4	3
4	265.0	6
6	231.2	18
8	148.0	21
10	83.1	23
12	46.9	25
14	27.5	33
16	16.4	39

RUNS 23,24,25 - 5/10/91

Propellant: nitrogen
Power: 63.5 W
Mass Flow Rate: 6.8E-5 kg/s
Stagnation Pressure: 6183 Pa
Stagnation Temp.: 700 K
Probe: Pitot probe 2
Axial Position: 12 mm (Run 23)

Radial Position (mm)	Maximum Pitot Pressure (Pa)
0	192.3
1	192.3
2	192.7
3	193.1
4	192.1
5	187.5
6	175.9
7	156.3
8	132.7
9	109.3
10	88.5
11	71.9
12	58.7
13	48.3
14	39.7
15	33.2
16	28.1
17	23.7
18	20.1
19	17.2
20	14.9
21	12.9
22	11.3
23	9.9
24	8.7

Axial Position: 24 mm (Run 24)

Radial Position (mm)	Maximum Pitot Pressure (Pa)
0	152.1
1	152.1
2	151.6
3	150.4
4	147.6
5	142.3
6	133.9
7	122.5
8	109.2
9	95.1
10	82.1
11	70.7
12	60.7
13	52.0
14	44.9
15	38.8
16	34.0
17	29.3
18	26.0
19	22.8
20	20.1
21	18.0
22	16.1
23	14.4
24	12.9

Axial Position: 36 mm (Run 25)

Radial Position (mm)	Maximum Pitot Pressure (Pa)
0	120.0
1	120.0
2	119.1
3	116.5
4	112.9
5	108.1
6	102.1
7	94.8
8	86.9
9	78.5
10	70.7
11	63.2
12	56.3
13	49.6
14	44.1
15	39.2
16	35.2
17	31.5
18	28.0
19	25.3
20	22.9
21	20.7
22	18.9
23	17.2
24	15.3

RUN 26 - 5/17/91

Propellant: nitrogen
Power: 63.5 W
Mass Flow Rate: 6.8E-5 kg/s
Stagnation Pressure: 6259 Pa
Stagnation Temp.: 700 K
Probe: Pitot probe 2
Axial Position: 12 mm

Radial Position (mm)	Max. Pitot Pressure (Pa)	Local Flow Angle (degrees)
0	191.3	0
2	191.7	2
4	191.5	3
6	176.1	7
8	133.1	12
10	89.2	17
12	59.6	18
14	40.5	22
16	28.4	25
18	20.4	29
20	15.2	34
22	11.5	38
24	8.8	42

Axial Position: 0 mm (Run 26)

Radial Position (mm)	Max. Pitot Pressure (Pa)	Local Flow Angle (degrees)
6	228.1	12

RUN 27 - 5/31/91

Propellant: nitrogen
Power: 63.5 W
Mass Flow Rate: 6.8E-5 kg/s
Stagnation Pressure: 6261 Pa
Stagnation Temp.: 700 K
Probe: conical probe 1
Axial Position: 0 mm

Radial Position (mm)	Cone Static Pressure (Pa)	Local Flow Angle (degrees)
0	21.61	0.0
2	21.16	1.8
4	17.87	6.3
5	14.76	10.3
6	11.60	14.8
7	8.80	19.1
8	6.56	23.7
9	4.77	-----
10	3.63	-----

RUN 28 - 6/7/91

Propellant: nitrogen
Power: 63.5 W
Mass Flow Rate: 6.8E-5 kg/s
Stagnation Pressure: 6263 Pa
Stagnation Temp.: 700 K
Probe: conical probe 1
Axial Position: 0 mm

Radial Position (mm)	Cone Static Pressure (Pa)	Local Flow Angle (degrees)
0	20.36	0
1	20.53	0.8
2	20.44	1.6
3	19.84	2.9
4	18.27	5.1
5	15.68	8.3
6	12.68	12.3
7	9.76	16.6
8	7.47	20.7
9	5.79	24.6
10	4.15	29.3

Axial Position: 12 mm (Run 28)

Radial Position (mm)	Cone Static Pressure (Pa)	Local Flow Angle (degrees)
6	10.21	9.7
8	6.85	15.7
12	3.15	25.4

RUN 29 - 6/14/91

Propellant: nitrogen
Power: 63.5 W
Mass Flow Rate: 6.8E-5 kg/s
Stagnation Pressure: 6234 Pa
Stagnation Temp.: 700 K
Probe: conical probe 1
Axial Position: 12 mm

Radial Position (mm)	Cone Static Pressure (Pa)	Local Flow Angle (degrees)
0	15.49	0
1	15.51	0.7
2	15.27	1.8
3	14.63	2.8
4	13.47	4.6
5	11.89	7.1
6	10.01	10.1
7	8.35	13.0
8	6.72	16.0
9	5.48	18.6
10	4.43	21.0
11	3.63	23.4
12	3.00	25.6
13	2.53	27.8
14	2.12	30.0
15	1.79	32.1
16	1.52	34.3
17	1.33	36.2
18	1.19	38.2
19	1.05	-----
20	0.95	-----

RUN 30 - 11/7/91

Propellant: nitrogen
Power: 63.5 W
Mass Flow Rate: 6.8E-5 kg/s
Stagnation Pressure: 6242 Pa
Stagnation Temp.: 700 K
Probe: conical probe 1 (2 static taps T-ed)
Axial Position: 12 mm

Radial Position (mm)	Cone Static Pressure (Pa)	Local Flow Angle (degrees)
0	17.93	0
4	14.43	9.5

RUN 31 - 3/5/92

Propellant: nitrogen
Power: 64.0 W
Mass Flow Rate: 6.8E-5 kg/s
Stagnation Pressure: 6414 Pa
Stagnation Temp.: 701 K
Probe: conical probe 1
Radial Position: 0 mm

Axial Position (mm)	Cone Stagnation Pressure (Pa)
0	263.6
6	220.2
12	189.2
18	165.3
24	148.0
30	131.3
36	116.9
42	102.9
48	90.7
54	78.9
60	68.0
75	50.1
100	31.9
125	22.3
150	16.8
200	10.1

RUN 32 - 3/6/92

Propellant: nitrogen
Power: 63.4 W
Mass Flow Rate: 6.8E-5 kg/s
Stagnation Pressure: 6425 Pa
Stagnation Temp.: 700 K
Probe: conical probe 1
Radial Position: 0 mm

Axial Position (mm)	Cone Stagnation Pressure (Pa)
-6	332.5
0	267.8
6	223.8
12	192.4
18	168.9
24	150.7
30	134.5
36	119.9
42	105.7
48	92.9
54	81.3
60	71.2
75	52.5
100	34.1
125	24.8
150	18.8
200	12.4
250	8.9
300	7.1
350	5.5
400	4.5
480	3.5

RUN 33 - 3/19/92

Propellant: nitrogen
Power: 64.1 W
Mass Flow Rate: 6.8E-5 kg/s
Stagnation Pressure: 6427 Pa
Stagnation Temp.: 700 K
Probe: conical probe 2
Axial Position: 12 mm

Radial Position (mm)	Cone Static Pressure (Pa)	Local Flow Angle (degrees)
0	16.84	0
2	16.09	2.1
4	13.24	6.2
6	9.01	12.4
8	5.60	18.2
10	3.47	22.9
12	2.23	27.1
14	1.47	30.8
16	1.00	34.3
18	0.71	37.1
20	0.53	39.3
24	0.37	41.1
28	0.31	39.1

Axial Position: 36 mm (Run 33)

Radial Position (mm)	Cone Static Pressure (Pa)	Local Flow Angle (degrees)
0	-----	0
4	7.69	5.8
8	4.99	11.6
12	2.95	16.4
16	1.77	20.1
20	1.13	23.0
24	0.77	25.4
28	0.56	27.1
32	0.44	27.8
36	0.37	27.7
40	0.33	26.9

Axial Position: 305 mm (Run 33)

Radial Position (mm)	Cone Static Pressure (Pa)	Local Flow Angle (degrees)
0	0.44	0

RUN 34 - 3/27/92

Propellant: nitrogen
Power: 64.6 W
Mass Flow Rate: 6.8E-5 kg/s
Stagnation Pressure: 6405 Pa
Stagnation Temp.: 700 K
Probe: conical probe 2
Axial Position: 12 mm

Radial Position (mm)	Cone Static Pressure (Pa)	Local Flow Angle (degrees)
0	16.79	0
2	15.96	2.1
4	13.11	6.1
6	8.96	12.1
8	5.56	18.0
10	3.40	22.8
12	2.12	27.3
14	1.35	31.7
16	0.87	35.9
18	0.57	40.0
20	0.40	44.0
24	0.20	50.2
28	0.15	55.0

Axial Position: 36 mm (Run 34)

Radial Position (mm)	Cone Static Pressure (Pa)	Local Flow Angle (degrees)
0	8.95	0
2	8.60	2.9
4	7.57	5.8
6	6.24	8.8
8	4.85	11.7
10	3.71	14.5
12	2.79	17.0
16	1.61	21.7
20	0.97	25.8
24	0.61	29.8
28	0.40	33.8
32	0.27	37.1
36	0.19	40.5
40	0.13	44.0

Axial Position: 100 mm (Run 34)

Radial Position (mm)	Cone Static Pressure (Pa)	Local Flow Angle (degrees)
0	2.12	0
5	2.04	3.5
10	1.80	6.8
20	1.11	12.8
30	0.61	17.7
40	0.35	22.3
50	0.20	26.5
60	0.13	30.0

RUN 35 - 4/2/92

Propellant: nitrogen
Power: 64.4 W
Mass Flow Rate: 6.8E-5 kg/s
Stagnation Pressure: 6413 Pa
Stagnation Temp.: 701 K
Probe: conical probe 2
Axial Position: 60 mm

Radial Position (mm)	Cone Static Pressure (Pa)	Local Flow Angle (degrees)
0	4.92	0
5	4.35	5.8
10	3.08	10.9
15	1.93	15.1
20	1.20	18.8
25	0.77	22.4
30	0.52	25.7
35	0.35	29.0
40	0.24	32.0
45	0.16	35.0
50	0.12	38.0
60	0.05	42.0

Axial Position: 60 mm (Run 35)
Radial Position: 30 mm

Rotary Position (degrees)	Cone Static Pressure 1 (Pa)	Cone Static Pressure 2 (Pa)
22	0.41	0.69
23	0.44	0.64
24	0.47	0.59
25	0.49	0.55
26	0.52	0.49
27	0.55	0.45
28	0.57	0.41
29	0.61	0.37
30	0.64	0.33

Axial Position: 80 mm (Run 35)

Radial Position (mm)	Cone Static Pressure (Pa)	Local Flow Angle (degrees)
0	-----	0
5	2.92	4.4
10	2.37	8.8
15	1.71	12.3
20	1.17	15.3
25	0.81	18.3
30	0.56	21.1
35	0.40	23.9
40	0.29	26.4
45	0.23	28.7
50	0.16	31.0
55	0.13	33.4
60	0.12	36.0

RUN 36 - 4/15/92

Propellant: nitrogen
Power: 64.6 W
Mass Flow Rate: 6.8E-5 kg/s
Stagnation Pressure: 6426 Pa
Stagnation Temp.: 700 K
Probe: conical probe 2
Axial Position: 120 mm

Radial Position (mm)	Cone Static Pressure (Pa)	Local Flow Angle (degrees)
0	1.65	0
5	1.60	3.1
10	1.47	5.9
15	1.25	8.6
20	1.03	11.0
25	0.81	13.1
30	0.64	15.3
35	0.51	17.1
40	0.40	18.5
45	0.33	20.3
50	0.28	22.4
55	0.23	24.7
60	0.20	27.0

Axial Position: 140 mm (Run 36)

Radial Position (mm)	Cone Static Pressure (Pa)	Local Flow Angle (degrees)
0	1.16	0
5	1.12	2.4
10	1.05	4.7
15	0.95	6.9
20	0.81	9.0
25	0.67	11.0
30	0.53	12.6
35	0.43	14.2
40	0.35	15.6
45	0.27	16.7
50	0.21	18.3
55	0.17	20.1
60	0.15	22.4

Axial Position: 160 mm (Run 36)

Radial Position (mm)	Cone Static Pressure (Pa)	Local Flow Angle (degrees)
0	0.92	0
5	0.89	2.0
10	0.87	4.0
15	0.80	6.0
20	0.72	7.9
25	0.63	9.7
30	0.53	11.6
35	0.44	13.1
40	0.36	14.6
45	0.31	15.9
50	0.25	17.3
55	0.21	19.0
60	0.17	20.7

Axial Position: 50 mm (Run 36)

Radial Position (mm)	Cone Static Pressure (Pa)	Local Flow Angle (degrees)
-30	0.45	-31.4
-25	0.71	-27.2
-20	1.16	-22.9
-15	2.07	-18.3
-10	3.68	-13.1
-5	5.81	-6.9
0	6.68	0
5	5.17	6.5
10	3.09	12.3
15	1.73	17.2
20	1.01	21.5
25	0.61	25.8
30	0.40	29.8

RUN 37 - 4/22/92

Propellant: nitrogen
Power: 67.0 W
Mass Flow Rate: 6.8E-5 kg/s
Stagnation Pressure: 6414 Pa
Stagnation Temp.: 700 K
Probe: conical probe 1
Axial Position: 100 mm

Radial Position (mm)	Cone Stagnation Pressure (Pa)
0	34.32
5	32.41
10	28.36
15	23.14
20	18.36
25	14.36
30	11.27
35	8.96
40	7.19
45	5.83
50	4.79
55	3.95
60	3.29

Axial Position: 120 mm (Run 37)

Radial Position (mm)	Cone Stagnation Pressure (Pa)
0	25.82
5	24.82
10	22.76
15	20.04
20	16.88
25	13.81
30	11.25
35	9.17
40	7.51
45	6.20
50	5.19
55	4.36
60	3.72

Axial Position: 140 mm (Run 37)

Radial Position (mm)	Cone Stagnation Pressure (Pa)
0	20.31
5	19.84
10	18.72
15	17.07
20	15.05
25	12.93
30	10.91
35	9.15
40	7.63
45	6.33
50	5.32
55	4.52
60	3.92

Axial Position: 160 mm (Run 37)

Radial Position (mm)	Cone Stagnation Pressure (Pa)
0	16.41
5	16.11
10	15.49
15	14.51
20	13.27
25	11.83
30	10.32
35	8.91
40	7.63
45	6.49
50	5.57
55	4.81
60	4.17

RUN 38 - 4/27/92

Propellant: nitrogen
Power: 64.2 W
Mass Flow Rate: 6.8E-5 kg/s
Stagnation Pressure: 6423 Pa
Stagnation Temp.: 700 K
Probe: conical probe 1
Axial Position: 100 mm

Radial Position (mm)	Cone Stagnation Pressure (Pa)
0	34.28
60	3.40

Axial Position: 120 mm (Run 38)

Radial Position (mm)	Cone Stagnation Pressure (Pa)
0	25.86
60	3.83

Axial Position: 140 mm (Run 38)

Radial Position (mm)	Cone Stagnation Pressure (Pa)
0	20.27
60	3.99

Axial Position: 160 mm (Run 38)

Radial Position (mm)	Cone Stagnation Pressure (Pa)
0	16.40
60	4.12

Axial Position: 60 mm (Run 38)

Radial Position (mm)	Cone Stagnation Pressure (Pa)
0	73.79
5	60.28
10	41.89
15	27.69
20	18.72
25	13.12
30	9.55
35	7.11
40	5.41
45	4.21
50	3.33
55	2.67
60	2.19

Axial Position: 80 mm (Run 38)

Radial Position (mm)	Cone Stagnation Pressure (Pa)
0	48.84
5	43.73
10	34.97
15	26.04
20	19.00
25	14.11
30	10.67
35	8.24
40	6.45
45	5.12
50	4.12
55	3.35
60	2.77

RUN 39 - 4/30/92

Propellant: nitrogen
Power: 64.9 W
Mass Flow Rate: 6.8E-5 kg/s
Stagnation Pressure: 6419 Pa
Stagnation Temp.: 700 K
Probe: conical probe 1
Axial Position: 12 mm

Radial Position (mm)	Cone Stagnation Pressure (Pa)
0	--------
5	142.11
10	43.37
15	16.45
20	7.25
25	3.27

Axial Position: 36 mm (Run 39)

Radial Position (mm)	Cone Stagnation Pressure (Pa)
0	123.54
5	90.25
10	47.86
15	25.80
20	15.43
25	9.84
30	6.61
35	4.59
40	3.29

Axial Position: 36 mm (Run 40)

Radial Position (mm)	Maximum Pitot Pressure (Pa)
0	119.07
5	86.13
10	42.46
15	20.57
20	11.25
25	6.81
30	4.47
35	3.08
40	2.21

RUN 40 - 5/5/92

Propellant: nitrogen
Power: 64.9 W
Mass Flow Rate: 6.8E-5 kg/s
Stagnation Pressure: 6425 Pa
Stagnation Temp.: 700 K
Probe: Pitot probe 3
Axial Position: 12 mm

Radial Position (mm)	Maximum Pitot Pressure (Pa)
0	--------
5	155.72
10	41.01
15	13.07
20	5.15
25	2.29

Axial Position: 60 mm (Run 40)

Radial Position (mm)	Maximum Pitot Pressure (Pa)
0	66.33
5	52.04
10	33.85
15	20.80
20	13.21
25	8.85
30	6.27
35	4.61
40	3.52
45	2.75
50	2.17
55	1.76
60	1.43

Axial Position: 80 mm (Run 40)

Radial Position (mm)	Maximum Pitot Pressure (Pa)
0	40.64
5	35.46
10	26.96
15	19.04
20	13.27
25	9.47
30	6.97
35	5.32
40	4.15
45	3.32
50	2.69
55	2.21
60	1.85

Axial Position: 120 mm (Run 40)

Radial Position (mm)	Maximum Pitot Pressure (Pa)
0	18.88
5	18.07
10	16.31
15	13.91
20	11.36
25	9.11
30	7.27
35	5.85
40	4.79
45	3.95
50	3.32
55	2.80
60	2.40

Axial Position: 100 mm (Run 40)

Radial Position (mm)	Maximum Pitot Pressure (Pa)
0	26.70
5	24.74
10	20.96
15	16.51
20	12.53
25	9.51
30	7.31
35	5.72
40	4.59
45	3.73
50	3.09
55	2.59
60	2.19

Axial Position: 140 mm (Run 40)

Radial Position (mm)	Maximum Pitot Pressure (Pa)
0	14.16
5	13.75
10	12.85
15	11.55
20	10.00
25	8.44
30	7.04
35	5.85
40	4.88
45	4.11
50	3.48
55	2.97
60	2.57

Axial Position: 160 mm (Run 40)

Radial Position (mm)	Maximum Pitot Pressure (Pa)
0	11.08
5	10.87
10	10.37
15	9.61
20	8.67
25	7.61
30	6.59
35	5.63
40	4.80
45	4.12
50	3.53
55	3.07
60	2.67

Radial Position: 0 mm (Run 40)

Axial Position (mm)	Maximum Pitot Pressure (Pa)
18	175.45
24	153.85
30	135.40
36	119.07
42	103.72
48	89.75
54	77.25
60	66.33
75	45.64
100	26.70
125	17.47
150	12.48
200	7.56
250	5.28
300	3.97
350	3.16
400	2.59
480	1.95

REPORT DOCUMENTATION PAGE

Form Approved
OMB No. 0704-0188

1. AGENCY USE ONLY (*Leave blank*)	2. REPORT DATE	3. REPORT TYPE AND DATES COVERED
	April 1993	Final Contractor Report

4. TITLE AND SUBTITLE

Experimentation in the Low-Density Plume of a Simulated Electrothermal Thruster for Computer Code Validation

5. FUNDING NUMBERS

WU–506–42–31
NAG3–577

6. AUTHOR(S)

Dana L. Meissner

7. PERFORMING ORGANIZATION NAME(S) AND ADDRESS(ES)

University of Toledo
College of Engineering
Toledo, Ohio 43606

8. PERFORMING ORGANIZATION REPORT NUMBER

E–7728

9. SPONSORING/MONITORING AGENCY NAMES(S) AND ADDRESS(ES)

National Aeronautics and Space Administration
Lewis Research Center
Cleveland, Ohio 44135–3191

10. SPONSORING/MONITORING AGENCY REPORT NUMBER

NASA CR–191112

11. SUPPLEMENTARY NOTES

Project Manager, P. Penko, Space PropulsionTechnology Division, (216) 977–7490.

12a. DISTRIBUTION/AVAILABILITY STATEMENT

Unclassified - Unlimited
Subject Category 20

12b. DISTRIBUTION CODE

13. ABSTRACT ***(Maximum 200 words)***

Pressures and flow angles are measured in the plume of a 20° half-angle, conical nozzle in vacuum with Pitot tubes and conical probes. The area of measurement in the plume ranges from the nozzle exit plane to 480 mm axially downstream and from the plume centerline to 60 mm radially. The nozzle has an exit-to-throat area ratio of 100:1 and a throat diameter of 3.2 mm. The nozzle flow exhausts to a vacuum of order 10^{-2} Pa to simulate a resistojet (an electrothermal rocket of less than 1 N of thrust) operating in space. Experimental data are given for flows of nitrogen at 55 and 68 mg/s, stagnation temperatures between 695 and 921 K, and stagnation pressures ranging from 5600 to 7100 Pa. Data are also given for argon at a rate of 68 mg/s, a stagnation temperature of 648 K, and stagnation pressures of 4500, 4750 and 4770 Pa. Measurements in the nitrogen plume are compared with computational results from a direct-simulation Monte Carlo method.

14. SUBJECT TERMS

Rarefied flow; Nozzle plume; Pitot pressure; Electrothermal thruster

15. NUMBER OF PAGES

80

16. PRICE CODE

A05

17. SECURITY CLASSIFICATION OF REPORT	18. SECURITY CLASSIFICATION OF THIS PAGE	19. SECURITY CLASSIFICATION OF ABSTRACT	20. LIMITATION OF ABSTRACT
Unclassified	Unclassified	Unclassified	